SLAC-423
SLAC/SSRL 0057
UC-410
(SSRL-M)

THE Si(100)-Sb 2x1 AND Ge(100)-Sb 2x1 SURFACES: A MULTI-TECHNIQUE STUDY

Matthew Richter

Stanford Linear Accelerator Center
Stanford Synchrotron Radiation Laboratory
Stanford University, Stanford, California 94309

August 1993

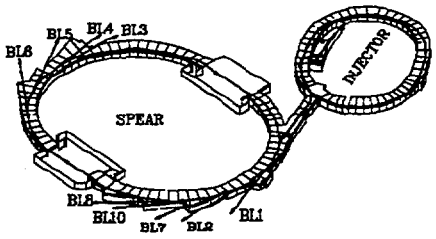

Prepared for the Department of Energy under contract number DE-AC03-76SF00515

Printed in the United States of America. Available from the National Technical Information Service, U.S. Department of Commerce, 5285 Port Royal Road, Springfield, Virginia 22161

---

* Ph.D. thesis

DISCLAIMER

DISCLAIMER

Portions of this document may be illegible in electronic image products. Images are produced from the best available original document.

Abstract

The electronic and geometric structures of the clean and Sb terminated Si(100)-2x1 and Ge(100)-2x1 surfaces have been investigated using a multi-technique approach. Low energy electron diffraction (LEED), scanning tunneling microscopy (STM), surface extended X-ray absorption fine structure (SEXAFS) spectroscopy and angle-integrated core-level photoemission electron spectroscopy (PES) were employed to measure the surface symmetry, defect structure, relevant bond lengths, atomic coordination and electronic structure. By employing a multi-technique approach, it is possible to correlate changes in the geometric structure to specific features of the core-level lineshape of the substrate. This allows for the assignment of components of the core-level lineshape to be assigned to specific surface and near-surface atoms.

We find that both the Si(100)-Sb and Ge(100)-Sb surfaces are comprised of Sb dimers. On the Si(100)-Sb surface, the Sb dimers have a Sb-Sb bond length of 2.91±0.03 Å. On the Si(100) surface each Sb atom is bonded to two Si atoms with a Sb-Si bond length of 2.63±0.03 Å. The bond lengths are given by the sum of the atoms covalent radii, 1.45 Å for Sb and 1.18 Å for Si. Tunneling microscopy observed and identified the defects present in the overlayer. These were voids and some slight second-layer occupation. STM also revealed that the size of the coherent domain is about 40 Å across. The presence of these anti-phase boundaries explains the weak intensities of second-order spots in the LEED pattern. Core-level photoemission shows a correlation between changes in the geometric and electronic structure of the surface. One of the surface peaks associated with one of atoms forming the Si dimers is eliminated upon Sb adsorption. The temperature dependence of the SEXAFS amplitude shows that the surface forms clusters if more than one monolayer is deposited. These clusters can be remove by annealing the sample at about 500°C, leaving a

well ordered, dimerized surface. All Sb desorbs when the sample is annealed at a temperature of 600°C.

The Ge(100)-Sb system behaves similarly with a few exceptions. The Sb-Sb dimer bond length is found to be 2.91±0.06 Å, while the Sb-Ge bond length is slightly shorter than the sum of covalent radii, measuring 2.58±0.06 Å. While STM was not performed on the Ge(100)-Sb system, the similar behavior of the LEED pattern suggests that anti-phase boundaries also play a significant role in the interfacial morphology. The Ge 3d core-level lineshape undergoes similar changes as the Si 2p core-level lineshape upon Sb deposition and ordered overlayer formation, allowing for similar assignments of particular surface and near-surface atoms to the various surface contributions to the overall Ge 3d lineshape. The most significant difference in behavior between the two systems is their evolution as a function of anneal temperature. While on the Si(100) substrate all excess Sb desorbs a temperature such that a well-ordered Sb overlayer remains, this is not the case on the Ge(100) substrate. At a temperature sufficient to desorb the excess Sb, the underlying Sb also starts to desorb, leaving a partially-covered Ge(100) surface.

This work also contains overviews of the relevant theories, paying special attention to the Transfer-Hamiltonian description of the STM by Tersoff and Hamann as well as $L_{2,3}$-edge SEXAFS theory. Our results are critically compared to other relevant literature.

To my family
and my friends.

Acknowledgments

My stay at Stanford has been a combination of exceeding satisfaction and unbelievable frustration, whose proportions I never could have imagined had I not experienced them myself. That is not to say that all the hardships were forced upon me. Many were of the self-inflicted variety! With a little more foresight on my part I could have avoided most of them completely. Stanford is a strange and wonderful place, and as a first-year graduate student, it was easy to become intimidated. As I learned the ropes and gained some expertise on how things got done here, I became much more effective as a researcher and a teacher. By far the most important lesson that I learned is that one *can not* do it all alone. In fact, I owe an immense debut of gratitude to all of those people who helped me with my ordeal.

First and foremost, I must thank Ingolf Lindau, my thesis advisor, for giving me a chance to succeed where others were skeptical. He found the time, and the money, to let me play my little vacuum games. Without that opportunity, I seriously doubt if I would have finished. I'm sure that at times I tried his patience, and I'm sure he knows that he's not the only one! Piero Pianetta has not only been a good research advisor, but he has become a good friend and at times, even an inspiration. I don't know how he does it, but he gets more done with less time each year, yet he never has lost that healthy irreverence for all things overly administrative and bureaucratic. I also would like to thank Dr. Walt Harrison for reading the thesis, and Dr. Dennis Bird for chairing at my orals.

I never could have done any successful experiments without the help of a few of my fellow students. Mike Green taught me how to work hard, and Joe Woicik taught me how to make a good measurement. Not only were they both instrumental in my development as a scientist, but they will remain good friends long into the future.

Tom Kendelewicz has always been willing to share his beam time, help with mine, and give me the benefit of his prodigious knowledge of semiconductor interfaces without a single complaint. Well, maybe a few little ones!

.All of my work has involved collaboration to some degree. First and foremost I must thank Jun Nogami without whose help this thesis would be much worse than it is. Ken Miyano, Joe, Tom and I had one of the loudest runs ever recorded in SSRL history, and it was my most succesfull one to boot! Jin Wu deserves recognition not only for helping with my PES data, but for surviving as my office-mate. No small feat there! And thank you Renyu Cao, for teaching me about photoemission.

I'd like to extend my apologies to everyone I made extra work for by not being on top of all my paperwork, especially Paula Perron, in the Department of Appled Physics. If not for her frequent prodding, I'm sure I'd have had to pay even more late fees than I did.

While the science is why we're here, the people are what make the stay satisfying. The early years here were always exciting with Jonny Henderson around. Bonnie Rippere kept me sane and happy when school wasn't fun anymore. I'm sorry that she couldn't be here at the finish. And to all the others who've had the luck, both good and bad, to spend some time in my company, you know who you are, and I thank you all.

Lastly, I have to thank my parents. Little did they know that they hadn't gotten rid of me for good when I went away to UCSD for my undergraduate degree. Mom, your cooking is too good to stay away from and there's never been a better, more willing technical proof-reader!

Table of Contents

List of Tables

List of Figures

1. Introduction

1.1 Overview and Motivation

The study of metal-semiconductor systems can shed light on many of the current questions in surface science.[1] These include information on the mechanisms of Schottky barrier formation, interfacial reactivity and morphology, as well as the attributes of metal-semiconductor interfaces in general. By measuring both geometric and electronic properties, we can also illustrate the interplay between geometric and electronic structure, providing concrete examples of their interdependence. It is becoming very apparent that the two are intimately intertwined and that many systems of interest in surface science cannot be understood without at least a basic knowledge of both. Unfortunately, most scientific techniques do not provide a diverse enough data set to determine completely the relevant properties of the system under study. In order to overcome this difficulty, combinations of low-energy electron diffraction (LEED), scanning tunneling microscopy (STM), surface-extended x-ray absorption fine structure (SEXAFS) spectroscopy and core-level photoemission electron spectroscopy (PES) were employed to measure both the geometric and electronic properties of two related interfaces.

The specific examples presented in this thesis involve the interaction of Sb, atomic number 51, with the (100) face of two column IV semiconductors, Si and Ge. This work originally started as an extension of the work on the Sb-Si(111) system of Woicik *et al.*[2] in which the combination of PES, SEXAFS and x-ray standing waves found that the absorption of one monolayer (ML) of Sb results in the removal of of the Si(111) 2x1 reconstruction and the formation of Sb trimers. These trimers are in the Milk Stool[3] geometry, with each Sb atom bonding covalently[4] to one Si and two Sb atoms.

Since that time it has also been found that Sb acts as a surfactant in the growth of epitaxial SiGe interfaces,[5–8] which are of much current interest. Without the use of a Sb buffer layer, layer-by-layer growth of Ge is limited to only two to three ML before clusters form and the interface no longer undergoes epitaxial growth.[9–11] Under these conditions, it is impossible to grow large-periodicity SiGe multilayers, which are also of considerable interest.

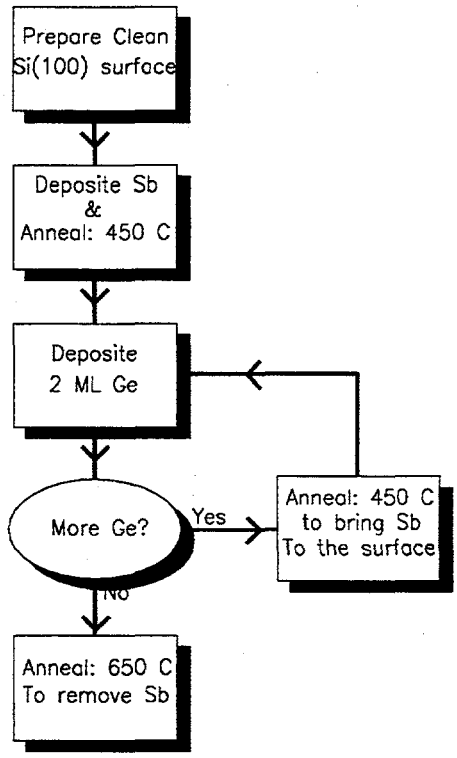

Figure 1. Sb assisted growth flow chart. The process used at Stanford to grow thick epitaxial Ge overlayers on Si substrates. Because the process is new, the working parameters have yet to be optimized.

If, on the other hand, one employs Sb as a surfactant, arbitrarily thick epitaxial layers of Ge theoretically can be grown.[5–8] A flow chart of the process under investigation here at Stanford is outlined in Fig. 1. Because the process is new, the optimal operating parameters and maximum obtainable overlayer thickness have yet to be determined. Nonetheless, epitaxial Ge layers 20 Å to 30 Å thick have already been grown. Bismuth (Bi), the element below Sb on the periodic table, has also been tried as an alternate surfactant, but didn't work as well. It is natural to ask why this is the case. A prerequisite to answering this question is the possession of an intimate knowledge of the Sb-Si(100) system, the substrate on which the Ge is grown.

Antimony is also a naturally occurring dopant of diamond,[12] and with the development of techniques that allow the growth of diamond thin films,[13–16] the Sb-diamond system has become a topic of current research.[17] Silicon, germanium and diamond are all tetrahedrally-coordinated semiconductors with different band gaps

and lattice constants (see Table 1). Antimony is a relatively large atom (its covalent radius is 1.45 Å) when compared to Si, Ge and especially C. This opens up the possibility of investigating the effect of substrate lattice size on overlayer geometry and electronic structure.

element	C	Si	Ge	Sb
bond length	1.54 Å	2.35 Å	2.44 Å	2.88 Å
(100) 2x1 area	12.68 Å^2	29.49 Å^2	31.79 Å^2	NA
band gap	5.5 eV	1.13 eV	0.76 eV	0.00 eV

Table 1. Properties of Sb, C, Ge and Si. Silicon, germanium and carbon all form tetrahedrally-coordinated semiconductors. This table lists several of the relevant properties of the various crystals. Note the much smaller size of the diamond lattice.

Advances in scientific understanding usually walk hand in hand with advances in experimental techniques. Because of this, this thesis follows two themes. The first theme concerns the measurement of specific properties of the systems under study. I want to find out: What are the relevant bond lengths? How does one produce a single-monolayer coverage of Sb on Si or Ge? How does the presence of the adsorbate modify the geometric structure of the surface? How does the adsorbate affect the electronic structure of the substrate? Is it possible to correlate the changes in electronic and geometric structure? What does this information imply about Sb's role as a surfactant? The second theme involves investigative techniques.

1.2 Techniques

While it is true that this thesis contains no new experimental technique *per se*, I demonstrate the power of combining several complementary techniques. It will be shown that by utilizing the combination of LEED, STM, SEXAFS and PES, complete and unambiguous determinations of the surface geometric and electronic structure can be made, even for systems whose structure could not be solved by one technique alone.

The STM was invented in 1982 by a group from IBM-Zurich[18] consisting of Gerd Binnig, Christoph Gerber, Ernst Weibel and Heini Rohrer, two of whom received the Nobel Prize for their work. This instrument is worthy of such recognition: people could actually "see" the atoms that form solids. While some other techniques have the abillity to image individual atoms or clusters in a few specific cases, the STM suffers from much fewer constraints: the sample must conduct electrons. The STM opened up a whole new world of surface science to research. Real-space information about surfaces on the atomic scale had previously been obtained only indirectly by area averaging techniques such as LEED, ion scattering, and a plethora of spectroscopies, including the two employed in this work, core-level PES, and SEXAFS spectroscopy.

The simplicity of the STM itself (it is just a very precise three-dimensional scanner and some equipment to hold a sample) and its relatively low initial cost[19] have allowed the field to grow at an exponential rate for the first five or so years. In fact, there are many related devices that have been invented based on the original STM design. These include low-temperature, ultra-high-vacuum, and electrochemical STMs; atomic force microscopy, employing an atomically sharp tip; scanning electropotential microscopy, employing a micro-capillary as the probe; scanning thermal microscopy, employing a miniature thermocouple. The whole group is collectively called scanning probe microscopy, along with its requisite acronym, SPM.

As with all new fields, STM went through a "looky here" stage where images of anything were new and exciting. Eventually, some shortcomings of the STM became apparent. As it turns out, STMs don't actually "see" atoms at all:[20] they image the charge density near the Fermi level (see Chapter 2 for STM theory). Therefore STM images are a convolution of both electronic and geometric structure. Eventually it became clear that while STMs did give real-space information about surfaces, some hard numbers were indeed lacking.

It was when I came to this realization that I began to be interested in some of the more conventional surface study techniques, and Stanford had this small synchrotron[21] in its backyard, so why not combine the two? While most of my early graduate years were spent doing tunneling microscopy in support of another student's thesis,[22] the bulk of my time has been spent doing more conventional synchrotron experiments in order to obtain these hard numbers that the STM fails to provide.

Since my interest is in geometric structure, it seemed natural for me to learn about SEXAFS spectroscopy and core-level PES. SEXAFS spectroscopy has been used as a structural probe since the late seventies.[23–25] It has the ability to measure bond lengths to a few hundredths of an Ångstrom, and coordination numbers and bond angles to about 20%. Because SEXAFS is a photoemission process,[26] it is chemically specific. It is also a short-range probe that does not require a sample with long-range order.

Core-level PES is also chemically specific[27–29] and does not require ordered systems. It is sensitive to the local potential that an emitting atom is located in and can therefore be used to infer information about geometric structure. Unfortunately, the number of components present in a given core-level lineshape gives only a lower limit to the number of chemically unique environments. It is possible that two peaks can lie so close together that it becomes impossible to resolve them. Since for kinetic energies of interest, the electron escape depth is less than 100 Å, PES is a surface probe, sampling the electronic structure of the first few atomic layers.

In order successfully to interpret the data from most experimental techniques, an intimate knowledge of both the details of data acquisition and underlying theory is required. Chapter 2 is concerned with the theories describing each technique. The knowledgeable reader can skip this chapter without losing any of the scientific content of this work. Although STM images comprise only a small portion of the

data presented here, the STM theory is presented in detail for two reasons. STM is a relatively young field and the theory is included for those unfamiliar with it. Also the Transfer Hamiltonian method is a very powerful technique for solving tunneling problems, and is included as a clear example of its power and simplicity.

Technique	**LEED**	**STM**	**SEXAFS**	**PES**
Probe Type	Area Averaging	Real Space	Area Averaging	Area Averaging
Min. Domain	100 Å	None	Nearest Neighbors	None
Chem. Specific	No	No	Yes	Yes
Bond Lengths	Poor	Poor	Excellent	Poor
Surface Symmetry	Excellent	Excellent	Good	Poor
Defect Identity	Poor	Excellent	Poor	Poor
Substrate Registry	Good	Good	Excellent	Poor
Elec. Structure	Poor	Poor	Poor	Excellent

Table 2. Summary of LEED, STM, PES and SEXAFS spectroscopies' relative strengths and weaknesses. Please note that STM is the only real-space probe, and as such is sensitive to individual defects. These defects contribute only to the background of the area-averaging techniques.

SEXAFS[30–32] and PES theory are both well established and relatively complete when compared to STM theory. Chapter 2 contains overviews of both theories, paying special attention to the specific parts that are relevant to this work. In the case of SEXAFS theory, multiple final-state effects are explicitly considered. The Three-Step Model[33] for photoemission is described, with special attention paid to those points that are of concern in angle-integrated core-level photoemission.

While there are many systems for which any one of these techniques can provide a unique description of the surface geometric structure, this is often not the case for subjects of current interest. Adatom-adatom bonding can make data analysis and interpretation difficult for both STM and SEXAFS while PES data can be interpreted in many ways. Because core-level PES gives only a lower limit to the number of chemically distinct sites, it is best used as an independent check of the geometric

structure as determined by either STM or SEXAFS or both. The relative strengths and weaknesses of the techniques are summarized in Table 2.

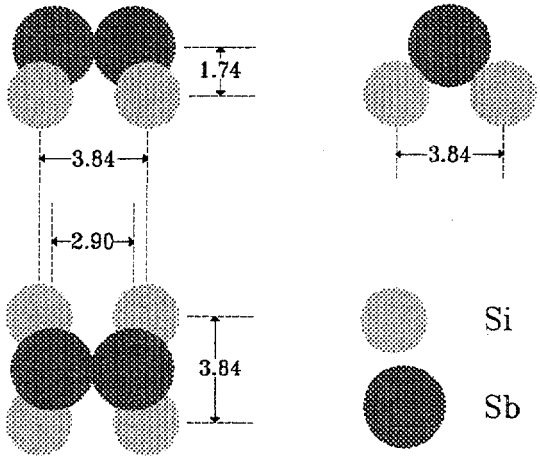

Figure 2. Sb forms dimers on both the Si(100) and Ge(100) surfaces. The bonding is covalent in nature, as determined by EXAFS spectroscopy. Each Sb atom is bonded to one other Sb and two substrate atoms. Basic electron counting suggests that the surface is fairly passive.

1.3 Experiments

Chapter 3 deals with the Sb-Si(100) system as studied by LEED, STM, SEXAFS and core-level PES, while Chapter 4 is a combined LEED, SEXAFS and PES study of the Sb-Ge(100) system. Each system is critically examined and compared to relevant literature. While these chapters are much more specialized than this introductory chapter, it is possible to get the fundamental ideas and conclusions by reading the first and last section of each of these chapters without being overwhelmed by specialized vocabulary.

The results presented in both chapters are surprisingly similar. Using the multi-technique approach, we find on both Si(100) and Ge(100) that Sb forms dimers on an unreconstructed substrate. All the bond lengths, Sb-Sb, Sb-Si, and Sb-Ge, are given

simply by the sum of covalent radii, within experimental error. Figure 2 shows the atomic position of Sb dimers on the (100) substrate. The electronic structure of both substrates undergoes similar changes upon Sb absorption and dimer formation. The multi-technique approach allows us to correlate these electronic changes to specific changes in the interfacial geometry.

The last chapter combines the conclusions of the previous two with other results from the literature, paying special attention to the trends that this work suggests. I will also discuss the natural extensions to this work, and address the validity of the assumptions made in the data analysis.

2. STM, SEXAFS and PES Theory

2.1 Introduction

Most experimental techniques require an intimate knowledge of both the details of data acquisition and underlying theory in order to interpret the results successfully. Therefore in this chapter I will present the relevant theories that pertain to this work. Because tunneling microscopy is a relatively new field, I will present STM theory in detail. Both SEXAFS and core-level PES are much more established, so only reviews of their theories will be presented here.

The technique used to model the STM, the Transfer Hamiltonion method, is a simple yet extremely powerful technique. Its application to the STM provides an elegant example of how it can be used to solve a relatively complicated tunneling problem. The results of the calculation give an understanding of just what the STM sees and how electronic structure and geometric structure are combined in the images. While the calculation presented here considers only the case of elastic tunneling, extensions can easily be made to include inelastic events.[34]

As previously mentioned, both SEXAFS and PES theory are much better established than that of STM. For this reason, I will present an overview of both theories, paying special attention to the specific parts that are relevant to this work. In the case of EXAFS theory, I will cover the effects of p-symmetry initial states and show how this leads to a decrease in the searchlight effect intensity. For the case of PES theory, I will briefly cover the three-step model of the photoemission process while focusing on the parts that pertain to core-level spectroscopy.

2.2 Scanning Tunneling Microscopy

The STM is capable of delivering images of surfaces with atomic resolution. But there are some cases where the images obtained do not correspond to the true geometric structure of the sample. Therefore after I explain what a tunneling microscope is and how it functions, I will discuss the details of STM theory and how they affect image interpretation.

The physical microscope is surprisingly simple. It consists of two components: A three-dimensional transducer that allows very precise positioning of a sharp tip relative to the sample surface; and something to hold the sample. Typically the transducer is made of a piezoelectric material, in the shape of either a tripod[18] or a tube.[35] The tip is usually attached to the scanner, but this isn't always the case. A drawing of a rather simple, yet productive STM developed here at SSRL is shown in Fig. 3. It consists of a rigid stainless-steel body, a differential micrometer used for sample approach, and a piezoelectric tube scanner to position the tip. Six wires are required to bring in all the voltages to the scanner, and one lead is used to extract the tunneling current.

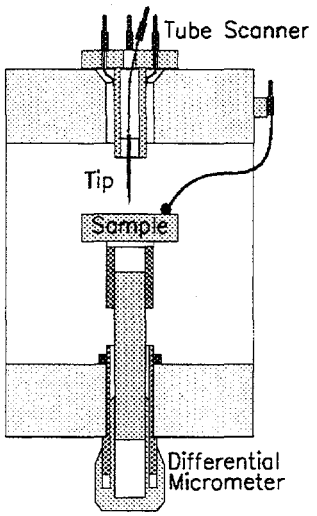

Figure 3. The SSRL air STM. The STM consists of a steel body, a differential micrometer, and a piezoelectric tube scanner. The symmetry of the steel body helps to minimize thermal drift while providing shielding for the AC signals that drive the scanner.

Since the STM must be able to position a tip with a precision of less than 0.1 Å, care must be taken to isolate the microscope head from external vibrations. This

particular microscope uses stainless steel plates separated by Viton riding on an air table to achieve the necessary isolation. The microscope used to obtain the images of the Sb-Si(100) surface shown in Chapter 3 employs a two-stage spring system with eddy current damping as its vibration isolation mechanism.[37] For a detailed analysis of its response and the stability of STMs in general, please see Park.[36]

A block diagram of the whole STM system is shown in Fig. 4. For STMs, the parameter used as a feedback signal to control the tunneling gap is the tunneling current. The tunneling current, typically from pico- to nanoamperes, is amplified and compared to the desired current. If the measured current is greater than the desired current, the tip-to-sample distance is increased. Conversely, if it is too small, the tip-to-sample distance is decreased. The simplest form is strictly proportional feedback, but a combination of integral and proportional is much more common.

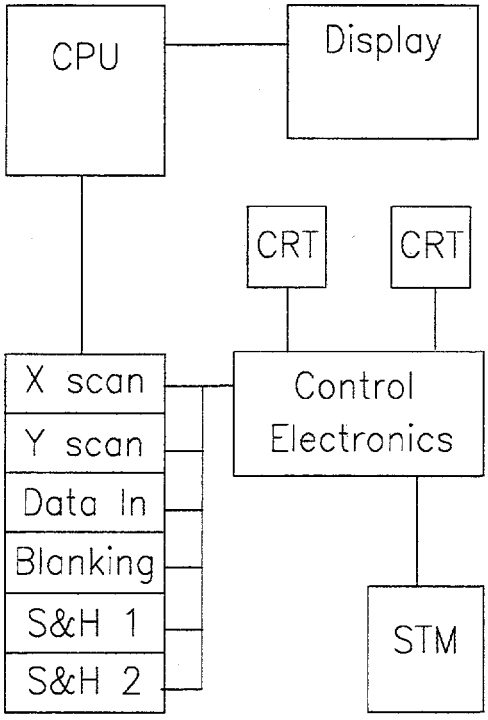

Figure 4. The SSRL STM control electronics. This schematic shows the fundamental units that comprise a STM. Scans are generated and data are collected by the computer. The electronics control the feedback loop, scan size and offset, along with some signal-conditioning electronics used to improve both image quality and dynamic STM performance. The two CRT displays are used to show the current trace, along with the instantaneous current and feedback response.

The tip is scanned in a raster pattern. The computer generates the signals that drive the x and y scans and the z position, the tip-to-sample distance, or the tunneling current is recorded as a function of x and y positions. If the feedback is set such that the instantaneous current is equal to the set current, this is known as *constant current imaging.* If the feedback parameters are set such that the average current is equal to the set current, one

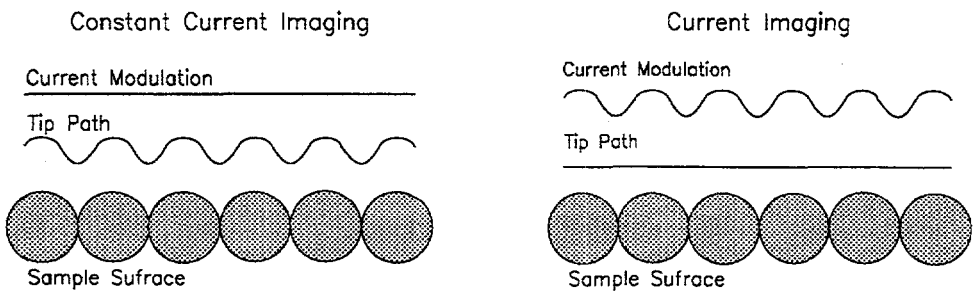

Figure 5. STM imaging modes. *Constant current imaging* provides a map of constant $\rho(E_F + eV, X, Y, Z)$, while *current imaging* measures $\rho(E_F + eV, X, Y)$ for a constant Z distance from the surface. While constant current imaging does provide quantitative information on vertical as well as horizontal information, one must keep in mind that since the STM images only a small portion of the total charge density, density of states effects may be very large.

can record the instantaneous current and obtain an image of the surface. This is know as *current imaging.* Because less bandwidth is required for current imaging, higher scan rates are possible, decreasing image aquisition time. The drawback of this technique is that one records only current intensities, and vertical displacements cannot be measured. The two techniques are depicted in Fig. 5.

Whatever signal is chosen for imaging, it must be amplified and offset in order to maximize the signal-to-noise ratio and hence, obtain the best possible image. This is analogous to using the contrast and brightness control on a video monitor. Unfortunately, the effects of this can drastically alter the image, making accurate image interpretation difficult or impossible.

Once an image is obtained, there are several post-acquisition image processing options available. Glitch removal can be used to remove spikes in the data. Background removal can be used to eliminate any slope to the image. Digital filtering, curvature mapping, and false shadows can all be used to enhance the visual content of the image. As thermal drift is often a problem in STM systems, the images can be sheared to eliminate this effect. All these tricks are used to improve the image quality so that it is easier to obtain *qualitative* information of the surface. The STM

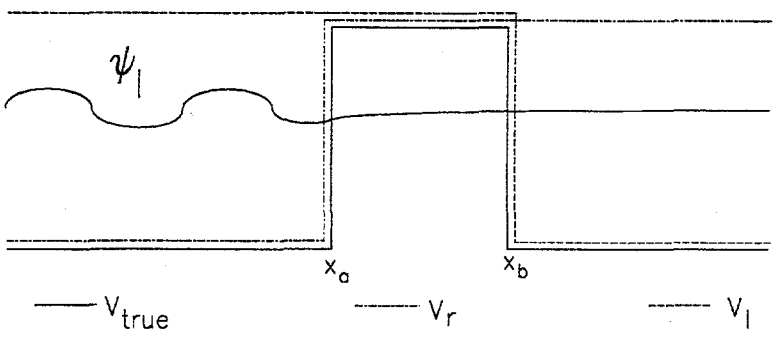

Figure 6. The Transfer-Hamiltonian method. The total potential for the square barrier is denoted V in the figure. The derivation extends to arbitrary barriers. The two potentials used as a starting point for the Transfer Hamiltonian calculation are designated V_r and V_l. The wave functions, Ψ_r and Ψ_l, associated with V_r and V_l are assumed to be known. These wave functions are non-orthogonal eigenfunctions of different Hamiltonians. Only Ψ_l is shown for clarity.

is invaluable in observing such things as atomic vacancies, dislocations and individual adatoms. We can now observe surfaces in intimate detail in a way never before possible.

Quantitative information is harder to come by. The easiest numbers to extract are lateral dimensions. If the STM is operating in constant current mode, vertical displacements can also be measured. But because the STM is sensitive to only a small fraction of the total charge density (explained below), the step height measured of an adsorbate layer may not be the true step height. In fact, there are some cases, most notably GaAs(110), where the STM sees only half the atoms.[39] In order to understand why this happens, we must examine the three-dimensional tunneling theory that describes STM operation.

The most intuitive theory that describes STM operation was developed by Tersoff and Hamann.[20] They employ the Transfer Hamiltonian method first published by Bardeen[40] to describe the tunneling process. Before I present the Tersoff-Hamann theory, I will present a brief review of the Transfer Hamiltonian method.

Consider, for simplicity, the square potential barrier shown in Fig. 6. The cal-

culation assumes that the wave functions for both the isolated systems, V_r and V_l, are known and are designated Ψ_r and Ψ_l, respectively. Note that Ψ_r and Ψ_l are non-orthogonal eigenstates of different Hamiltonians. The exact eigenstate of the full potential can be written as the following superposition of states:

$$\Psi = a\Psi_l e^{-i\omega_l t} + \sum_r b_r \Psi_r e^{-i\omega_r t} \tag{2.1}$$

where $\omega_{r,l} \equiv \frac{E_{r,l}}{\hbar}$ and both a and b_r are time dependent. Substitution into the Schrödinger Equation yields

$$\begin{aligned} H\Psi &= i\hbar\frac{\partial}{\partial t}\Psi \\ &= (aE_l + i\hbar\dot{a})\Psi_l e^{-i\omega_l t} + \sum_r (b_r E_r + i\hbar\dot{b}_r)\Psi_r e^{-i\omega_r t}. \end{aligned} \tag{2.2}$$

At $t = 0$, $a = 1$, $b_r = 0$ and $H\Psi = H\Psi_l e^{-i\omega_l t}$, therefore,

$$H\Psi_l e^{-i\omega_l t} = E_l \Psi_l e^{-i\omega_l t} + \sum_r i\hbar\dot{b}_r \Psi_r e^{-i\omega_r t}. \tag{2.3}$$

If we require that the transition is elastic, we obtain

$$i\hbar\sum_r \dot{b}_r \Psi_r = (H - E_l)\Psi_l. \tag{2.4}$$

Multiplication by Ψ_r^* and integration over all space produces

$$i\hbar\dot{b} = M_{lr} = \int_{-\infty}^{\infty} \Psi_r^*(H - E_l)\Psi_l dx, \tag{2.5}$$

where we have introduced the tunneling matrix element M_{lr}. Because Eq. (2.5) is non-zero only for $x > x_b$, we can change the lower limit of integration to x'

from $-\infty$, where x' is contained in the boundary region (see Fig. 6). Because $(H - E_r)\Psi_r^* \equiv 0$ for $x > x_a$, we can symmetrize the integral as follows

$$M_{lr} = \int_{x'}^{\infty} \left(\Psi_r^* \left(H - E_l\right) \Psi_l - \Psi_l \left(H - E_r\right) \Psi_r^*\right) dx. \tag{2.6}$$

Integration by parts yields

$$M_{lr} = \frac{\hbar^2}{2m} \left(\Psi_r^* \frac{d}{dx} \Psi_l - \Psi_l \frac{d}{dx} \Psi_r^* \right) \Big|_{x'}. \tag{2.7}$$

The three-dimensional extension of this is

$$M_{lr} = \frac{\hbar^2}{2m} \int_S d\vec{S} \cdot \left(\Psi_r^* \nabla \Psi_l - \Psi_l \nabla \Psi_r^*\right) \tag{2.8}$$

where the surface S is defined to lie completely within the boundary where $V_r = V_l = V$. It is important to note that the dimensionality of the problem has been reduced by one.

Bardeen then invokes Fermi's Golden Rule

$$\begin{aligned} P_r(E) &= \frac{2\pi}{\hbar} \left|M_{lr}\right|^2 \nu_l(E) \\ &= \frac{2\pi}{\hbar} \sum_l \left|M_{lr}\right|^2 [1 - f(E_l + eV)] \delta(E_l - E) \end{aligned} \tag{2.9}$$

where $\nu_l(E)$ is the density of states as a function of energy and $f(E)$ is the Fermi function. The total current is obtained by summing over contributing states along with their occupation, and multiplying by the electronic charge, e. Therefore

$$I = \frac{2\pi e}{\hbar} \sum_{l,r} \left|M_{lr}\right|^2 f(E_r)[1 - f(E_l + eV)] \delta(E_l - E_r). \tag{2.10}$$

This general expression for the tunneling current is the starting point for the Tersoff-Hamann theory.

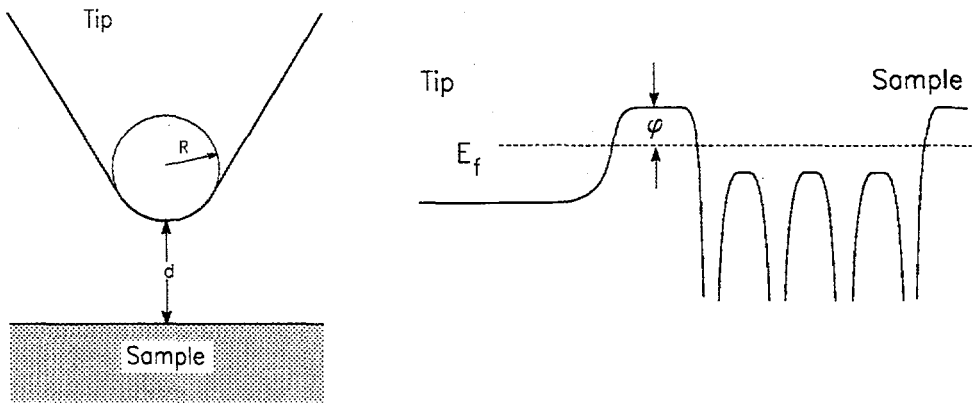

Figure 7. The geometry of the Tersoff-Hamann model of the STM. The tip radius is taken to be R, and the tip-to-sample distance is d. A one-dimensional representation of the total potential used in the calculation is shown on the left.

For simplicity, T-H assume tunneling between identical metals. The derivation is similar in the case of dissimilar sample and tip materials. If $eV \ll \phi$ and $kT \ll E_f$, where ϕ is the work function and E_f is the Fermi Energy, Eq. (2.10) can be written as

$$I = \frac{2\pi e^2 V}{\hbar} \sum_{l,r} |M_{lr}|^2 \delta(E_l - E_f)\delta(E_r - E_f). \tag{2.11}$$

Now all that remains is to calculate M_{lr}.

At the time Tersoff and Hamann wrote their paper, the structure of the tip was not well known, and they modeled their tip as a spherical potential, shown in Fig. 7. This gives us normalized tip wave functions, Ψ_t, of the form

$$\Psi_t = Re^{\kappa R}\Omega_t^{-1/2}\frac{e^{-\kappa r}}{r} \tag{2.12}$$

where Ω_t is the tip volume and $\kappa = \sqrt{\frac{2m}{\hbar^2}e\phi}$ where ϕ is the work function of the tip. For this expression, the center of curvature of the tip is taken as the origin.

T-H expand both the tip wave functions and those of the sample by Fourier transforming the wave functions and then solving for the matrix elements by working

in the $\vec{k}$ regime. In a modification to the T-H theory, Herring[41] uses a much more elegant derivation presented here.

Herring defines new functions, Ψ_t', that are identically equal to Ψ_t for $|\vec{r}| > R$. The difference between the functions is that for $|\vec{r}| < R$, Ψ_t' is still defined and well behaved. This analytic continuation allows us to deform the surface of integration, S, into a small sphere, S_o, centered about $\vec{r}_o$, the center of the original tip. The new geometry is shown in Fig. 8. Now let's examine each term in the matrix element, Eq. (2.8), using the new wave functions Ψ_t'. Starting with the second term,

$$\begin{aligned}\int_S d\vec{S}\cdot\Psi_t\nabla\Psi_s^* &= \int_S d\vec{S}\cdot\Psi_t'\nabla\Psi_s^* \\ &= \int_{S_o} d\vec{S}\cdot\Psi_t'\nabla\Psi_s^* \\ &= \int_{S_o} |d\vec{S}||\Psi_t'\nabla\Psi_s^*|.\end{aligned} \tag{2.13}$$

In the limit that $r_o \to 0$,

$$\begin{aligned}\lim_{r_o\to 0}\int_{S_o} |d\vec{S}||\Psi_t'\nabla\Psi_s^*| &= \lim_{r_o\to 0} 4\pi r_0^2\left|\Psi_t'(r_o)\nabla\Psi_s^*|_{r_o}\right| \\ &= \lim_{r_o\to 0} 4\pi r_0^2 R e^{\kappa R}\Omega_t^{-1/2}\frac{e^{-\kappa r_o}}{r_o}\left|\nabla\Psi_s^*|_{r_o}\right| \\ &\propto \lim_{r_o\to 0} r_o e^{-\kappa r_o} \\ &= 0.\end{aligned} \tag{2.14}$$

Therefore, we can combine Eq. (2.13) and Eq. (2.14) to show

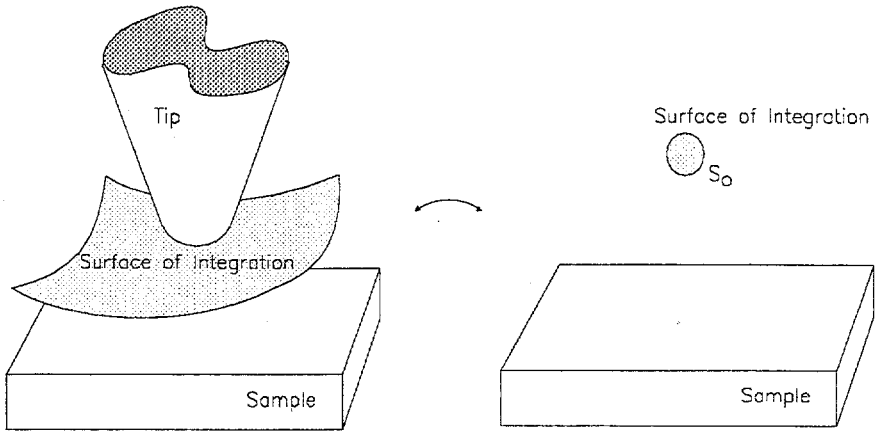

Figure 8. Evaluation of M_{lr}. Because the surface of integration is arbitrary in evaluating M_{lr}, we can preform an analytic continuation of the original tip wave function that is valid for $|\vec{r}| < R$. Then we can deform the surface of integration to be a small sphere, S_o, centered about the tip's original center of curvature. While the physics is invariant under these transformations, the mathematics is greatly simplfied.

$$\begin{aligned} M_{lr} &= \frac{\hbar^2}{2m}\int_S d\vec{S}\cdot(\Psi_s^*\nabla\Psi_t - \Psi_t\nabla\Psi_s^*) \\ &= \frac{\hbar^2}{2m}\int_S d\vec{S}\cdot\Psi_s^*\nabla\Psi_t \\ &= \frac{\hbar^2}{2m}\int_{S_o} d\vec{S}\cdot\Psi_s^*\nabla\Psi_t^l \\ &= \frac{\hbar^2}{2m}\int_{S_o} dS\Psi_s^*\frac{\partial}{\partial r}Re^{\kappa R}\Omega_t^{-1/2}\frac{e^{-\kappa r}}{r}. \end{aligned} \tag{2.15}$$

Once again, in the limit $r_o \to 0$,

$$\begin{aligned} M_{lr} &= \lim_{r_o\to 0}\frac{\hbar^2}{2m}\int_{S_o} dS\Psi_s^*\frac{\partial}{\partial r}Re^{\kappa R}\Omega_t^{-1/2}\frac{e^{-\kappa r}}{r} \\ &= -\frac{2\pi\hbar^2 Re^{\kappa R}}{m\Omega_t^{1/2}}\lim_{r_o\to 0}\Psi_s^*(r_o)(1+\kappa r_o)e^{-\kappa r_o} \\ &= -\frac{2\pi\hbar^2 Re^{\kappa R}}{m\Omega_t^{1/2}}\Psi_s^*(0). \end{aligned} \tag{2.16}$$

Substitution of (2.16) into Eq. (2.11) yields the tunneling current for the Tersoff-Hamann model of the STM:

$$I = 8\pi^3\hbar^3 e^2 V R^2 e^{2\kappa R} m^{-1}\Omega_t^{-1} D_t(E_f)\rho_s(0, E_f), \tag{2.17}$$

where $\rho_s(0, E_f) = \sum_s |\Psi_s^*(0)|^2\delta(E_s - E_f)$. The term $D_t(E_f)$ is the density of contributing tip states.

From the final expression for the tunneling current, we now can see why the STM may not see some of the atoms. The STM images only the charge density very near to the Fermi energy. On a polar semiconductor such as GaAs, the states on either side are associated with only one type of atom. At certain bias voltages, there may be no states available to tunnel into or out of. The STM wouldn't see anything whereas an AFM, which is sensitive to total charge density, would see an atom. The GaAs system is a very drastic example of how electronic structure can and does affect STM images. Therefore, it is very important to keep in mind the electronic structure of the sample in question when examining STM images.

In order to understand more about STM behavior, it proves useful to examine the behavior of the sample wavefunction near, but external to, the surface. In general a surface may be represented by a two-dimensional square barrier.[42] We can write the sample wavefunction as the following summation

$$\Psi(\vec{r}, \vec{k}) = \sum_{k_\parallel} e^{i\vec{k}_\parallel\cdot\vec{r}} f_{k_\parallel}(z) \tag{2.18}$$

where $k_\parallel$ designates the wave vector parallel to the surface. Substitution of Eq. (2.18) into the Schrödinger equation yields

$$-\frac{\hbar^2}{2m}(k_\parallel^2 + \frac{d^2}{dz^2}) f_{k_\parallel}(z) + (V - E) f_{k_\parallel}(z) = 0. \tag{2.19}$$

Therefore

$$f_{k_\parallel}(z) \propto e^{-\sqrt{k_\parallel^2+\kappa^2}z}. \tag{2.20}$$

We can now see that $\vec{k}_\parallel$ acts to dampen out higher-frequency components of the wave function. For STM, this implies that as the tip gets farther from the surface, the corrugation ought to be nearly sinusoidal. For $\vec{k}_\parallel = 0$, $f_0(z) \propto e^{-\kappa z}$. In Fig. 7, $z = R + d$. Since $\rho \propto \Psi^2$, $\rho \propto e^{-2\kappa(R+d)}$. Combining this with the previously-derived result for the tunneling current, Eq. (2.17), shows us that $I \propto e^{2\kappa R}e^{-2\kappa(R+d)}$ or, more simply,

$$I \propto e^{-2\kappa d}. \tag{2.21}$$

The exponential dependence on the tip radius, R, has been eliminated. The tunneling current, I, is now only exponentially dependent on d. This exponential dependence on d makes the exact value of the leading constant rather unimportant. The main features of the theory are as follows: The tunneling current is linear in the applied voltage, for small biases. The current is exponentially dependent on the tip-to-sample distance. Further, and most significant, the current is proportional to the density of states of the sample at the Fermi Energy.

While the theory is tractable, it does have some problems. The Tersoff-Hamann approach assumes that the basis set of wave functions that satisfy the Schrödinger Equation in an isolated sample or tip do not change when the tip-sample system is considered as a whole. This assumption ignores two things: it does not take the effect of an image charge into account; second, it ignores the fact that the tunneling process takes place in very high fields. Typically tunneling voltages are on the order of volts. The typical tip-to-sample separation distance is about 10 Å, resulting in field gradients of about $10^9 V/m$. These fields are several orders of magnitude above those required for field emission, and must have some effect on the tunneling barrier

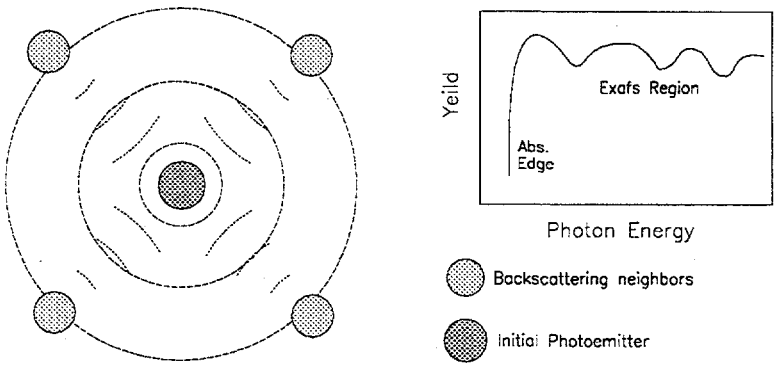

Figure 9. The EXAFS mechanism. The emitted photoelectron scatters off neighboring atoms. As the electron's kinetic energy is increased, the reflected wave's amplitude at the position of the original photoemitter sweeps through nodes and anti-nodes. This results in a modulation of the photoabsorption coefficient. This modulation results in an oscillatory behavior on the high-energy side of an atomic absorbtion edge, known as EXAFS.

as well as the charge density of the surface in the vicinity of the tip. There is evidence that the tip-sample interaction is much stronger than assumed. In the case of simple metals, standard solid-state calculations predict modulation intensities for the charge density of states near the Fermi energy to be on the order of a few hundredths of an Ångstroms, less than the resolution of most STMs. Many groups have succeeded in imaging metal surfaces with atomic resolution, in contradiction to the T-H result. Further, Tersoff and Hamann present some qualitative arguments that allow them to ignore tip states of non-s symmetry, but they fail to treat these assumptions explicitly.

Despite these flaws, there are some cases where the agreement is remarkable. Tersoff and Hamann used the radius of the tip and the tip-to-sample distance as adjustable parameters to fit some of the early STM data on the Au(110) 2x1 surface. The best fit was obtained assuming a tip radius of 9 Å and a tip-to-sample distance of 6 Å. Using these values, they predicted a modulation amplitude of 1.4 Å for the Au(110) 3x1 surface reconstruction, in excellent agreement with experiment.

Despite the quantitative agreement in the above sample, we must look to other techniques to obtain bond lengths and atomic coordination. Both these quantities can

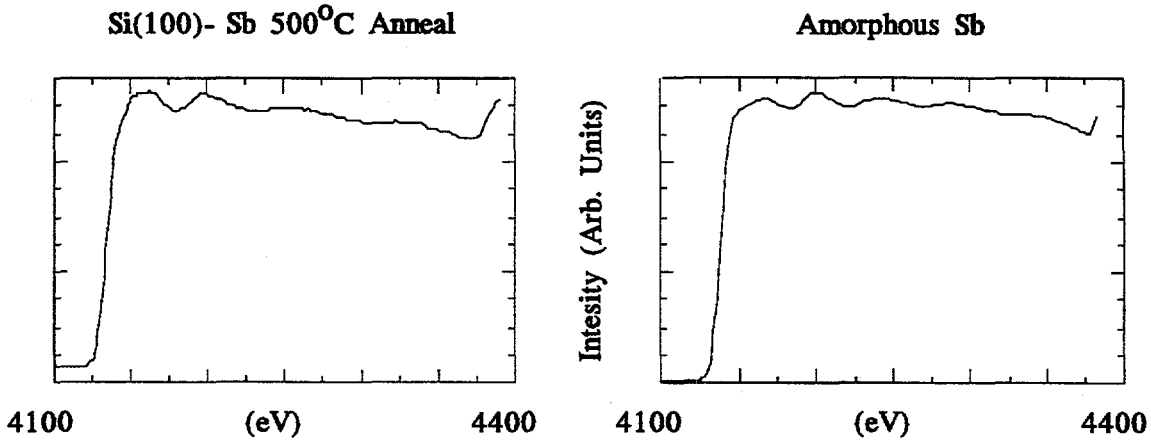

Figure 10. EXAFS frequency *vs.* bond length. These two Sb L_3-edge electron yield spectra are from amorphous antimony (right) and a single monolayer of Sb deposited on the Si(100) 2x1 surface annealed at 500° C (left). These two spectra illustrate the inverse relation between bond length and EXAFS wavelength. The longer-wavelength oscillations in the left spectrum originate from the shorter Sb-Si bond than the oscillations, due to Sb-Sb bonding, in the right spectrum. The Sb-Sb bond length is 2.90 Å while the Sb-Si bond is 2.63 Å.

be obtained very accurately using extended x-ray absorption fine structure (EXAFS) spectroscopy.

2.3 Extended X-Ray Absorption Fine Structure Spectroscopy

In conventional X-ray absorption experiments, a large drop in the transmitted flux occurs when the incoming photon energy is swept through the threshold of one of the sample's electron binding energies, or core levels. This is known as an absorption edge. For incident photon energies above the absorption edge, a photoelectron is created. If the emitting atom is bonded to any neighbors, the outgoing photoelectron can scatter, and the scattered and outgoing wavefunctions can interfere either constructively or destructively, modifying the matrix element governing the original photoemission event. This interference, or EXAFS, manifests itself as an oscillatory behavior on the high energy side of an absorption edge. This interference is illustrated in Fig. 9.

Since EXAFS theory is fairly well understood and there are many good reviews

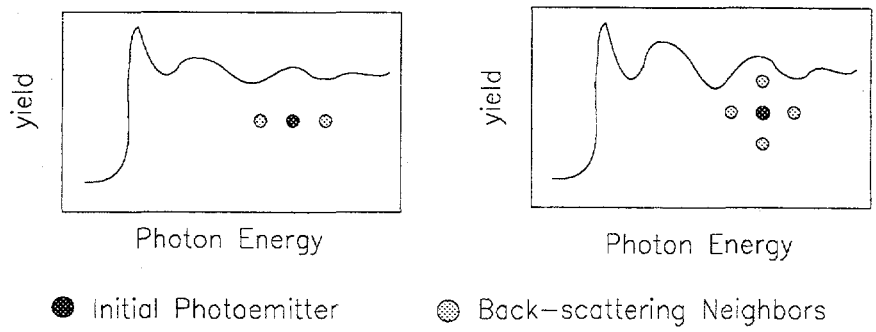

Figure 11. EXAFS frequency *vs.* number of neighbors. The effect of the number of neighboring atoms on the EXAFS amplitude is shown. The case of four neighbors will have twice the amplitude than the case where the photoemitter only has two.

on EXAFS theory available, I will focus only on the highlights of EXAFS theory. I will also explain the differences between K or L_1, and $L_{2,3}$-edge EXAFS and the difficulty that multiple final states can cause. Those interested in a complete theoretical description of EXAFS theory are referred to references 30 to 32. The $L_{2,3}$-edge EXAFS theory is based on the work of Citrin.[43]

The wavelength of the EXAFS oscillation depends on the interatomic distance. For longer bonds, shorter wavelength oscillations are observed, and vice versa. This is illustrated in Fig. 10. The amplitude is determined by the number of neighbors, among other things. This is shown in Fig. 11. Because EXAFS contains information about both bond length and coordination, it is an excellent technique to apply to the study of geometric structure, of both bulk substances and surfaces. Since EXAFS experiments require a tunable source of photons, it was only with the availability of synchrotron radiation that EXAFS has been widely used.

Before the oscillations can be analyzed, they must be isolated. This is accomplished by first subtracting the background, and then normalizing the oscillation to the absorption spectrum that would be obtained from the isolated atom. Experimentally, this is

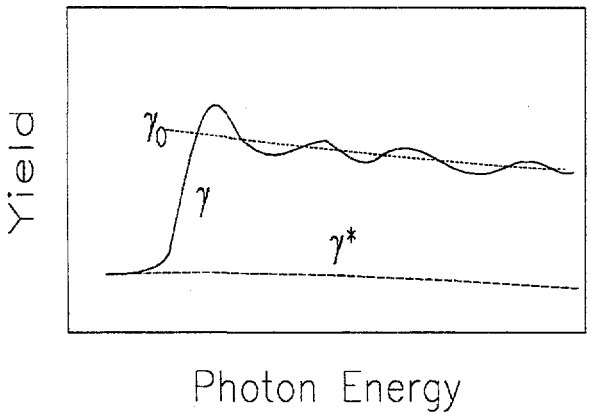

Figure 12. EXAFS background subtraction. This figure show how the EXAFS is isolated. Experimentally, the EXAFS is given by $\chi(h\nu) = \frac{\gamma-\gamma_0}{\gamma_0-\gamma^*}$ where γ is the measured spectrum, γ^* is the background function and γ_0 is the absorption spectrum of the isolated atom. γ_0 is approximated using a spline fit to the data.

$$\chi(h\nu) = \frac{\gamma - \gamma_0}{\gamma_0 - \gamma^*} \tag{2.22}$$

where γ is the measured spectrum, γ^* is the background function and γ_0 is the absorption spectrum of the isolated atom. The spectrum γ_0 is approximated using a spline function. The isolation of the EXAFS oscillations is shown in Fig. 12. For photon energies within about 50 eV of the absorption edge, multiple scattering cannot be ignored. At higher energies, a single scattering model can be used to accurately analyze the data.

The single-scattering EXAFS equation for states of initial s symmetry is

$$\chi(k) = -\sum_j \frac{N_j}{kR_j^{-2}} f_j(\pi, k) \sin\Big(2kR_j + \phi_j(k)\Big) e^{-2\sigma_j^2 k^2} e^{-R_j/\lambda(k)} \tag{2.23}$$

where the sum is over neighboring shells of N_j atoms at a distance R_j. The term $f_j(\pi, k)$ is the backscattering amplitude, which is specific to the atomic species of the j^{th} shell. The argument of the sine factor is the total phase of the backscattered wave due to path distance and phase shift from the core potentials of the photoemitting and backscattering atoms. The term $e^{-2\sigma_j^2 k^2}$, where σ_j is the mean square displacement of

the scatterer from its ideal position, is a Debey-Waller-like correction that takes into account the thermal vibration of the atoms and is temperature dependent. Another term is also included, $e^{-R_j/\lambda(k)}$, where $\lambda(k)$ is the electron mean free path, that takes into account the loss of phase information due to inelastic scattering.

Since $\chi(k) \propto f_j(k)$, we can "fingerprint" the EXAFS signal. The backscattering amplitudes for both oxygen and molybdenum are a case in point. For $k < 6$ Å^{-1}, the two amplitudes are comparable. At 10 Å^{-1}, the Mo amplitude is a factor 6.5 times larger. If any EXAFS oscillations are observed near 10 Å^{-1} or higher, one can conclude that this is mostly due to scattering from Mo neighbors. While this is indeed qualitative, fingerprinting bonds can be used to draw conclusions where EXAFS cannot be collected over a wide enough k range to allow detailed quantitative analysis. In Chapters 3 and 4 we will use this technique to support the conclusions drawn from the analysis of the Sb L_3-edge data.

The application of the EXAFS technique to surfaces requires some modification of Eq. (2.23). Synchrotron radiation is highly polarized and we must take this effect into account. In the derivation of the Eq. (2.23), an integration over all polarizations is performed. The removal of this step only affects the amplitude of the EXAFS oscillations. This is known as the *searchlight effect*. This leads to the replacement of N_j with N_j^* in the EXAFS equation. The term N_j^* is known as the effective coordination number for states of initial s symmetry and is defined as follows:

$$N_j^* = 3 \sum_i^{N_j} \cos^2 \alpha_j \tag{2.24}$$

where α_j is the angle formed between the polarization vector of the synchrotron light and the vector formed between the original photoemitter and the i^{th} backscatterer of the j^{th} shell. The factor 3 is included so that integration over all polarizations yield N_j.

Consider the geometry illustrated in Fig. 13. For the first shell, the adatom has only one neighbor, i.e. $N_1 = 1$. For $\alpha_i = 0$, $N_j^* = 3$. Conversely, for $\alpha_i = \frac{\pi}{2}$, $N_j^* = 0$. This anisotropy is the basis for bond angle determination in surface EXAFS (SEXAFS). It is convenient to define the relative effective coordination number to be the ratio of two effective coordination numbers. In the case of this simple geometry, the relative effective coordination number ranges from infinity to zero. The use of relative effective coordination numbers allows data to be analyzed without resort to model compounds, removing a possible source of error (see below). In practice, both absolute and relative effective coordination numbers must be used in order to determine an absorption site uniquely.

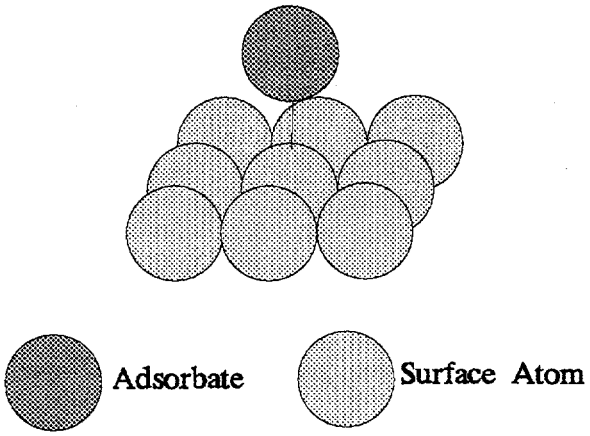

Figure 13. The Searchlight effect. For the geometry shown, the effective K or L_1edge coordination number can vary from zero to three, depending on the orientation of the polarization vector of the incoming light. The relative effective coordination number, formed by taking the ratio of two effective coordination numbers obtained at different polarization angles, exhibits even more drastic effects, varying from zero to infinity.

It is not always the case that the K or L_1 edge can be used in an experiment. For heavy atoms, the K edge is at many tens of thousands of eV. In some cases, such as Pd,[44] Coster-Kronig relaxation dominates and the L_1 edge lacks sufficient intensity for practical use. One must keep in mind the range of available photons when choosing which edge to use. In the case of antimony, only the L_3 edge could be used for quantitative analysis. Therefore I will go over the differences encountered when dealing with $L_{2,3}$ edge EXAFS.

For states of initial s symmetry, K and L_1 edges, the dipole selection rule dictates that the final state of an adsorption process must have p symmetry. States of initial

p symmetry, L_2 or L_3 edges, can have both s or d final state symmetry. In order to accurately analyze EXAFS data from L_2 or L_3 edges, these effects must be taken into account. Citrin[43] has treated this case explicitly to find that

$$\begin{aligned}\chi(k,\theta) = A(k)\Big(&n_d(\theta)\sin\big(2kR+\phi_{2b}(k)\big) + n_s\sin\big(2kR+\phi_{0b}(k)\big)\\ &+ n_{sd}\sin\big(2kR+\phi_{2b}(k)+\delta_a(k)\big)\Big)\end{aligned} \tag{2.25}$$

where

$$\begin{aligned} n_d(\theta) &= 0.5\Big(\frac{2}{2+c^2}\Big)\sum_{i=1}^{N}(1+3\cos^2\alpha_i)\\ n_s &= 0.5\Big(\frac{c^2}{2+c^2}\Big)\\ n_{sd}(\theta) &= \Big(\frac{2c}{2+c^2}\Big)\sum_{i=1}^{N}(1-3\cos^2\alpha_i). \end{aligned}$$

While Citrin points out that these quantities can be thought of as effective *partial* coordination numbers, he also states that the physical analogy present in the K-edge theory is lost due to the fact that n_{sd} can take on negative values. The quantity c has been calculated[45] to be 0.2 for $Z \geq 20$ and it is only weakly dependent on k. Using this value for c, and taking $c^2 \approx 0$, we find that Eq. (2.25) becomes

$$\chi(k,\theta) \approx A(k)\Big(n_d(\theta)\sin\big(2kR+\phi_{2b}(k)\big) + n_{sd}\sin\big(2kR+\phi_{2b}(k)+\delta_a(k)\big)\Big) \tag{2.26}$$

with

$$\begin{aligned} n_d(\theta) &\approx 0.5\sum_{i=1}^{N}(1+3\cos^2\alpha_i)\\ n_{sd}(\theta) &\approx 0.2\sum_{i=1}^{N}(1-3\cos^2\alpha_i). \end{aligned}$$

There is an angle between the surface normal and the polarization vector of the incoming light, 54.7°, which for surfaces of three-fold symmetry or higher,[46] is called the *magic angle*, for which $n_{sd} \equiv 0$. Then the $L_{2,3}$ edge case becomes formally

equivalent to the K-edge theory with the replacement of the effective coordination number, N^*, with n_d. This has the sole effect of reducing the anisotropy in the angular dependence of the EXAFS amplitude. Because no knowledge of the phase term δ_a is required at this angle, bond lengths can be extracted without concern that multiple final-state effects will cause any error. For off-magic-angle data, the assumption that $\delta_a = 0$ leads to the relation

$$\chi(k,\theta) \approx A(k)N'(\theta)\sin\left(2kR + \phi_{2b}(k)\right) \tag{2.27}$$

where

$$N'(\theta) \approx \sum_{i=1}^{N}\left(0.7 + 0.9\cos^2\alpha_i\right). \tag{2.28}$$

The angular dependence of the EXAFS amplitude has been further reduced. The errors introduced by the assumption $\delta_a = 0$ can lead to erroneous absolute effective coordination numbers that can cause errors in absorption site determination.[47] The use of both relative and absolute effective coordination numbers can reduce or eliminate these errors.[48] These errors along with the decrease in EXAFS angular dependence are motivating reasons to perform multi-technique experiments to determine the true absorption site.

Once the data are collected and the EXAFS isolated, $\chi(E)$ is mapped into k-space, and then Fourier-transformed into R space. The EXAFS from model compounds is also Fourier-transformed. The contributions from the various shells are isolated by Fourier filtering. Since the bond lengths and coordination are known for the model compounds, their backscattering amplitudes and phase shifts can be extracted numerically. These parameters are then used to fit the Fourier-filtered data from the sample under examination, using the bond length, R_j, and the effective coordination number, N_j^*, as fitting parameters. These can be compared to theoretical values

calculated from assumed possible absorption site geometries to determine the atomic position. Concrete examples of this procedure are shown in Chapters 3 and 4.

To review, SEXAFS can, in optimal cases, determine bond lengths very accurately, typically to a few tenths of an Ångstrom. Chemically-specific coordination information can also be obtained. Further, since EXAFS is a short-range probe, the systems studied need not exhibit long-range order. The drawback of the technique is that it is an area-averaging technique, and as such can give no information on the nature of defects. In some cases where $L_{2,3}$ edges are all that are available for study, errors can be induced by the assumptions used in data analysis. When combined with STM, however, an independent check can be used to see if the errors are indeed significant for the system under study. Further, the complementary nature of the data obtained from both techniques leads to a complete description of the geometric structure of the sample.

2.4 Photoemission Electron Spectroscopy

Photoemission electron spectroscopy (PES) is also an area-averaging technique. The sample under study is exposed to a source of photons, in this work a synchrotron, and the electrons emitted are collected and analyzed. The photoemission process is dependent on many parameters, specifically the incoming light energy, angle of incidence, and polarization, along with the emitted electron's kinetic energy, angle of emission, and spin polarization. Different properties of the sample can be probed depending on which parameters are controlled in the experiment. For solid samples, this process is usually described by the three step process[33], described in Fig. 13, involving the initial photoionization, the transport of the electron to the surface, and its final escape into vacuum.

We can model the three-step process as follows. The experimentally observed

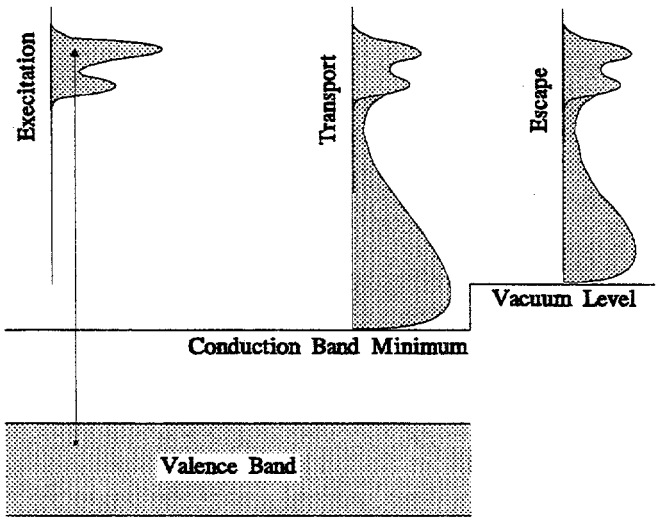

Figure 14. The Three-Step Model. The three-step model of photoemission from solids breaks the photoemission process into independent components. The first step is the initial photoionization. The second step involves the emitted electrons' transport to the surface and the creation of the inelastic tail, and the last step describes the electrons' escape into vacuum.

electron distribution curve (EDC), $N(E)$, can be written as

$$N(E) = AN_o(E)L(E)T(E) \tag{2.29}$$

where $N_o(E)$ is the electron distribution in the sample after the initial photoionization process, $L(E)$ describes the transport of the electrons to the surface, and $T(E)$ describes the electrons' escape into vacuum.

The distribution $N_o(E)$ is proportional to both the density of states (DOS) in the sample, along with their occupation and the photoionization cross section. Quantum mechanically, this cross section is given by

$$\sigma_{nl}(h\nu) = \frac{4}{3}\pi^2\alpha a_o^2\Big(N_{nl}(E-E_{nl})\frac{1}{2l+1}\Big)\Big(lR^2_{E,l-1}+(l+1)R^2_{E,l-1}\Big) \tag{2.30}$$

where

$$h\nu = E + E_{nl}$$

$$\alpha = \text{the fine structure constant}$$

$$a_o = \text{the Bohr radius}$$

$$N_{nl} = \text{the number of electrons in the subshell}$$

$$E_{nl} = \text{the binding energy}$$

$$E = \text{the kinetic energy of the emitted electron}$$

and the radial dipole matrix elements, $R_{E,l\pm1}$, are given by

$$R_{E,l\pm1} = \int_0^\infty P_{nl}(r) \cdot r \cdot P_{E,l\pm1}(r) dr \tag{2.31}$$

where $r^{-1}P_{nl}(r)$ is the radial part of the atomic wave function. The energy dependence of the photoionization cross section greatly influences the electron distribution curves obtained experimentally. Tabulated values of $\sigma_{nl}(h\nu)$ are readily available.[49]

Because the photon absorption coefficient is relatively small, the decay length, $\alpha(h\nu)$, of the incident photons is much larger than the escape depth of the electrons, $l(E)$, from the solid.[50] Therefore only a fraction of the exited electrons can escape into the vacuum without undergoing scattering. We can define a transport function, $L(E)$, such that

$$L(E) = l(E) \cdot \alpha(h\nu). \tag{2.32}$$

This proportionality to the electron escape depth is the key to the surface sensitivity of photoemission. Our expression $L(E)$ takes into account only elastic photoelectrons. The hot electrons inside the solid can undergo scattering, creating a cascade of secondary electrons. Some of these secondary electrons escape into vacuum and may be collected. This phenomenon adds an inelastic "tail" upon which the elastic EDC

is superimposed. In practice, as long as the features of interest in the EDC are on a fairly slowly varying region of the inelastic tail, the background is subtracted before analysis.

The term $T(E)$ is a smooth function and does not introduce significant structure to the EDC, and is of no consequence for this work.

The total core-level lineshape is comprised of an intrinsic core-level lineshape characteristic of the perfect crystal, along with other components that may be shifted relative to the bulk peak. These shifts have their origins in the local potential felt by the emitting atom. If an atom is bonded to different atomic species than the rest of the atoms in the crystal, this can result in a chemical shift. Our interest lies in both chemical shifts and shifts induced by a geometrical rearrangement of the atoms, such as those near a surface or interface. Termination of a lattice will result in a different potential at the surface compared to that in the bulk. The relaxations or reconstructions present at the surface also cause a redistribution of charge that results in changing potentials at the surface.

If these shifted components are at different depths, their relative intensities will change as we probe different photon energies, and hence, different escape depths. Or if two shifted peaks have the identical relative intensities as a function of photon energy, we can infer that there are two distinct environments for atoms at that depth. If the two peaks have relative intensities that change as a function of escape depth, we can infer which is closer to or at the surface.

The overall core-level lineshape depends on several factors. Spin-orbit splitting can separate the core-level into multiple peaks, with relative amplitudes proportional to the branching ratio. The shape of each singlet can be approximated by the convolution of a gaussian curve, representing a combination of resolution and thermal

smearing, and a lorenzian curve, due to lifetime broadening.

Analysis of core-level lineshapes involves extracting the gaussian and lorenzian widths from a bulk-sensitive spectrum and using these to fit the surface-sensitive spectrum. It is often the case that the bulk-sensitive spectrum still has an appreciable surface contribution. Therefore the fitting procedure is usually iterative, being complete when relative peak positions and intensities are consistent with each other and with the escape depth of the collected electrons.

There are cases where this procedure fails. If the shifted components are too close together, sometimes the resolution is insufficient to separate the two. If, however, the intrinsic linewidth has been obtained independently, these values can be used to fit the data and resolve shifted components that the conventional curve-fitting technique failed to resolve. One way to obtain these linewidths is by the use of a terminating overlayer. This technique was pioneered by Woicik[51] and Kendelewicz.[52] While it is true that the intrinsic linewidth may be smaller than that obtained by the use of the termination overlayer, it cannot be greater. In Chapter 3, I employ this technique to resolve previously unobserved interfacial components in the Si(100)-Sb system.

2.5 Multi-Technique Studies

In this chapter, I have outlined the relevant theories describing each technique. Here I will review the strengths and weaknesses of each technique and show how multi-technique studies can help eliminate the ambiguities in any single technique.

STM is the only real-space probe discussed. As such, it has a distinct advantage over both SEXAFS and PES in the identification of surface defects and mid-range order. Unfortunately, electronic-structure effects can make data interpretation difficult or misleading. Another important consideration is that the STM images states near the Fermi energy. These states are difficult to associate with individual atomic species

and because of this, one must assume the chemical identity of the atoms observed. In the case of weakly-interacting systems this may not pose a problem, but in general this is not the case.

SEXAFS and PES are area-averaging techniques, and as such are capable of far greater resolution by summing the signals of many equivalent sites. Both techniques are also chemically specific. This specificity is obtained by tuning the photon energy to a specific atomic core level.

SEXAFS can, in the best of cases, determine bond lengths to approximately 0.02 Å, and coordination numbers to about 20%. The searchlight effect and bond "fingerprinting" can also give information on bond angles that can lead to unique absorption site determination. Because SEXAFS is a short-range probe, long-range order is not required.

In the case of $L_{2,3}$-edge SEXAFS, the angular dependence of the EXAFS amplitude is diminished, leading to possible errors in absorption site assignment. This problem is further compounded by assumptions made about the scattering phase shifts. While for many systems this may not pose significant problems, this is not clear *a priori.*

Core-level photoemission spectroscopy gives information about the number of unique sites as a function of depth into the sample. Besides providing an independent check of the surface geometric structure as determined by STM and SEXAFS, PES is a probe of electronic structure. Its use in combination with one or more structural probes allows the correlation of geometric structure with specific features of the electronic structure, illuminating the interplay between the two.

The next two chapters show concrete examples of the interplay between the techniques as well as the complementary nature of the data from each. Chapter 3 applies

all three techniques to the Sb-Si(100) system. Chapter 4 is concerned with the combination of LEED, PES and SEXAFS as applied to the Sb-Ge(100) system.

3. The Si(100)-2x1 Sb Interface

3.1 Introduction

The Sb-semiconductor interface system has recently become a significant topic in surface science. Antimony (Sb) has been investigated as a delta-dopant in column IV semiconductors,[53] and is one of the only naturally-occurring dopants in diamond.[12] It has also been shown to act as a surfactant, or buffer layer, in the growth of thick epitaxial overlayers and heterostructures.[5-8]

Currently, efforts are focused on Sb's role as a surfactant in the growth of thick epitaxial germanium (Ge) overlayers on silicon (Si) substrates.[6-8] Without the use of a Sb buffer layer, one can grow only two to three Ge monolayers (ML) before clusters form and the interface no longer undergoes layer-by-layer growth. Under these conditions, it is impossible to grow large-periodicity SiGe multilayers, which are also of considerable interest.

Our choice of the Sb-Si(100) system was motivated by the above considerations. Along with the quest for scientific understanding, we can also demonstrate the power of multi-technique studies. Using a combination of real-space and spectroscopic techniques, we will completely characterize the geometric structure of the system and correlate changes in the electronic structure to specific geometric features of the interface, providing a unique glimpse into the sub-nanoscale world.

Before delving into the details of our measurements, it proves fruitful to examine some results from other similar systems, namely the As-Si(100) and the Sb-Si(111) systems. This information, along with some early PES work on the Sb-Si(100) system itself, should shed some light on the Sb-Si(100) interface and aid in our data interpretation. Early work on the Sb-Si(100) system indicates that the formation of

a monolayer of Sb on the surface does not remove the Si dimers, providing a termination of the surface by saturating the surface dimer dangling bond.[54–56] While these studies do shed some light on the electronic structure of the system, they suffer from low resolution and do not provide a detailed picture of the geometric structure of the interface. In fact, it turns out that the geometric model invoked by the authors to explain their data is not correct. This is a concrete example of the dangers of attempting to determine geometric structure based on core-level lineshape analysis.

There is a very complete description of both the electronic and geometric structure of the Sb-Si(111) system.[3,47,48,57,58] It has been predicted theoretically and determined experimentally that Sb forms trimers in the milk-stool geometry. Each Sb atom has one filled dangling bond and is bonded to one Si and two Sb atoms. The atoms in the topmost Si layer are unreconstructed with four-fold coordination. The Si-Sb and Sb-Sb bonds are completely covalent, as determined by SEXAFS and XSW.[47,48]

The simplest geometric model possible for the Sb-Si(100) interface involves Sb atoms terminating an ideal unreconstructed Si lattice. Unfortunately, this geometry does not result in the minimum number of partially-filled dangling bonds. Each Sb atom would have three electrons in two dangling bonds. If the Sb atoms were to form dimers on an unreconstructed Si(100) surface, all partially-filled dangling bonds would be eliminated, although a small energy price is paid in straining the Sb-Si bonds. The topmost Si atoms would be four-fold coordinated. The Sb would be three-fold coordinated with one filled dangling bond, but with two Si and one Sb nearest neighbors. This will be referred to as the *Sb dimer model.* This would be very similar to the behavior of Sb on the Si(111) surface, on which the topmost Si atoms are four-fold coordinated, and all the dangling bonds are filled. An elegant study of the As-Si(100) interface by Zegenhagen *et al.*, employing x-ray standing waves,[59] found that arsenic, one row above Sb on the periodic table, forms dimers

on the surface, leaving the Si unreconstructed, lending support to our assumptions. They also report that the As dimer surface still exists after the deposition of 30 Å of amorphous As. This indicates that the surface is fairly passive, which simple electron counting would predict. STM has also observed large coherent domains of As dimers, practically free of defects.[60]

The differences between the Sb dimer model and the model suggested by Rich *et al.* in ref. 55 are many. Rich's model contains no Sb-Sb bonding, with the topmost Si atoms remaining reconstructed, bonding to three other Si atoms and only one Sb atom. In the Sb dimer model, the topmost Si atoms are also four-fold coordinated, but they are unreconstructed, no longer forming dimers. They each bond to two Si atoms in the layer below as well as to two Sb surface atoms. The presence of the Sb dimers also explains the origins of the 2x1 LEED pattern. Now we have a reasonable prediction of the overlayer geometry.

The adatom-adatom bonding present in the Sb-Si(111) system makes data interpretation for both SEXAFS and STM much more difficult. At the time of this experiment, STM images of the Sb-Si(111) surface had not yet shown the orientation of the trimer, or its registry.[57,58] In fact, the images identify only the periodicity of the surface. The cause of this lies in the fact that the STM could not resolve the individual atoms in the Sb trimers, nor could the registry of the trimers be determined experimentally by STM. The identification of the STM features as trimers in the milk-stool geometry was determined by total energy minimization calculations.[57] Because the Sb dimer model for the Sb-Si(100) system predicts adatom-adatom bonding, there is even more reason to perform a multi-technique study of the system.

The combination of STM, PES and SEXAFS gives a complete experimentally determined description of the Sb-Si(100) interface. We find that our assumptions are justified and that the surface is accurately described by the Sb dimer model. The Sb

dimers have a Sb-Sb bond length of 2.91±0.03 Å. Each Sb atom is bonded to two Si atoms with a Sb-Si bond length of 2.63±0.03 Å. These bonds are almost purely covalent, with the bond lengths given by the sum of the atoms' covalent radii, 1.45 Å for Sb and 1.18 Å for Si. Tunneling microscopy observed and identified the defects present in the overlayer. These were voids and some slight second layer occupation. STM also revealed that the size of the coherent domain is about 40 Å across. The presence of these anti-phase boundaries explains the weak intensities of second-order spots in the LEED pattern. Core-level photoemission shows a correlation between changes in the geometric and electronic structure of the surface. One of the surface peaks associated with the one of atoms forming the Si dimers is eliminated upon Sb adsorption. The temperature dependence of the SEXAFS amplitude shows that the surface forms clusters if more than one monolayer is deposited. These clusters can be remove by annealing the sample at about 500°C. All Sb desorbs when the sample is annealed at a temperature of 600°C.

The use of all three techniques allows the unambiguous quantitative determination of the surface electronic and geometric structure in which the strengths of one technique remove the uncertainty introduced due to the weaknesses of the other methods. STM provides a real-space image of the surface symmetry. STM images also provide us with information on the nature of the defects in the overlayer along with information on the medium-range order unattainable with any other technique. SEXAFS provides the hard numbers that STM never could, while the STM images eliminate the uncertainty introduced by several of the assumption made in SEXAFS data analysis. Photoemission electron spectroscopy correlates the geometric information obtained with the two structural probes to specific changes in the electronic structure of the substrate.

3.2 Experiment

The Si wafer samples were initially degassed for 6 hours at 600°C. The Si was heated to a temperature of 1150°C for 15 minutes. All temperatures were measured with an infrared pyrometer or a thermocouple attached to the manipulator head. Pressures during the sample heating did not exceed 1.5×10^{-9} torr. A sharp two domain 2x1 LEED pattern was observed. Auger electron spectroscopy (AES) showed the samples to be free of contamination. For the SEXAFS measurements, two monolayers (ML) of Sb were deposited at room temperature at a rate of 1 ML per minute and subsequently annealed at 375°C for 15 minutes. During deposition and annealing, the chamber pressure was held below 1×10^{-9} torr. LEED showed a 1x1 pattern with diffuse two-domain 2x1 spots. AES showed the presence of Sb, and no oxygen or carbon was detected. This sample preparation technique had previously been reported to desorb all but one monolayer of the Sb.[54,55] Our SEXAFS measurements indicated that while LEED implies that surfaces prepared using a 375°C anneal exhibit long-range order, bulk-like Sb-Sb bonding dominates the SEXAFS spectra. This will be discussed further below. In order to obtain a single ordered Sb overlayer, it was necessary to anneal the surface at 550°C for 15 minutes. This treatment also gave a 1x1 LEED pattern with diffuse two-domain 2x1 spots.

The SEXAFS data were recorded using the Jumbo double-crystal monochromator[61] at the Stanford Synchrotron Radiation Laboratory. The energy resolution of this monochromator is 1.9 eV at a photon energy of 4100 eV using Ge(111) crystals. The experimental chamber (base pressure better than 7×10^{-11} torr) consists of a main chamber housing LEED optics, a load lock system, and a double-pass cylindrical mirror analyzer (CMA), the axis of which lies along the polarization vector of the synchrotron radiation. The sample manipulator has an on-axis configuration which allows the sample normal to rotate in the plane formed by the CMA axis and

the direction of light propagation. Samples were prepared in an adjacent chamber equipped with an electron beam heater, Sb sources and a quartz crystal rate monitor. The samples were moved between the main chamber, the preparation chamber and the load lock system with magnetically coupled transfer arms.

The Sb L_3-edge SEXAFS were collected by monitoring the Sb $L_3M_{4,5}M_{4,5}$ Auger emission as a function of incident photon energy and flux in the constant final state mode.[62] Data were recorded at three different angles: glancing incidence has the polarization vector and surface normal forming an angle of 15°; magic angle[63] has the polarization vector and surface normal forming an angle of 55°; and normal incidence has the polarization vector and surface normal forming an angle of 75°.

The STM images were obtained in a separate UHV chamber housing the STM, LEED optics, evaporation sources and an electron beam heater. Samples were prepared for the STM in a similar manner as described above with Sb coverages ranging from 0.6 to 2 ML. The image shown below is for the 0.6 monolayer coverage. All STM data discussed were obtained from samples annealed at 550°C. The tunneling microscope used has been described elsewhere.[36,37]

The PES spectra were obtained on beamline 3-1, the New Grasshopper,[38] at SSRL, using the same chamber used for the SEXAFS study. The CMA employed, however, was not fitted with an electron gun. Therefore AES could not be used to check for contamination. PES of the clean surface indicated the presence of some oxygen, in the form of SiO_x, and no carbon was observed. Since the clean surface is only used for reference and the Sb-covered surfaces showed no oxygen contamination, this slight oxide can be ignored.

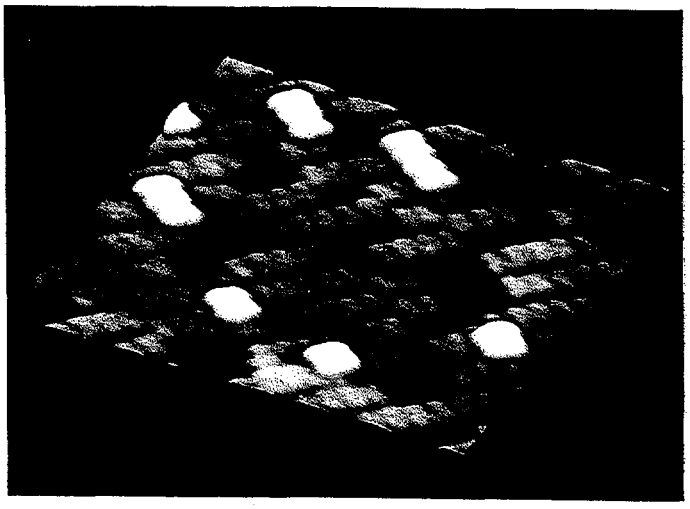

Figure 15. Si(100)-Sb STM image[71]. This constant current image of the Sb-Si(100) 2x1 surface shows a region of 60x60 Å^2. The tunneling current was 80 pA at a bias voltage of -1.3 V. The dimension of the oblong units, 3.8x7.6 Å^2, is consistent with Sb dimers. This image shows the power of STM in identifying the nature of defects at an atomic scale. There is some second-layer occupation, and depressions, presumably bare Si. The size of a coherent 2x1 domain is about 40 Å, providing a possible explanation of the weak second-order spots in the LEED pattern.

3.3 Scanning Tunneling Microscopy

It was not possible to image the sample prepared with a 375°C anneal. For this particular microscope, this indicates a clustered surfaces.[64] Annealing the sample to 550°C improved sample quality. Figure 14 shows a typical area of Sb coverage[71]. The image is 60 Å x 60 Å. It was taken in constant current mode with a tunneling current of 0.3 nA at a tip-to-sample bias of -1.2 V. Since the tip is at a lower potential than the sample, we are tunneling into the sample imaging unfilled states.

We can see that the surface is covered with oblong units, measuring 7.6x3.8 Å^2. This is the size of a surface dimer, within experimental accuracy. While there are still some uncovered areas of Si, there is not sufficient resolution to image the substrate, making it impossible to determine the overlayer registry, and hence, the surface atoms' coordination.

In fact, the chemical identity of the surface atoms is assumed to be Sb. While in this case there is no reason to assume otherwise, this is often not so. In the case of the more reactive Ag-Si systems, STM could not tell you if Ag or Si formed the topmost

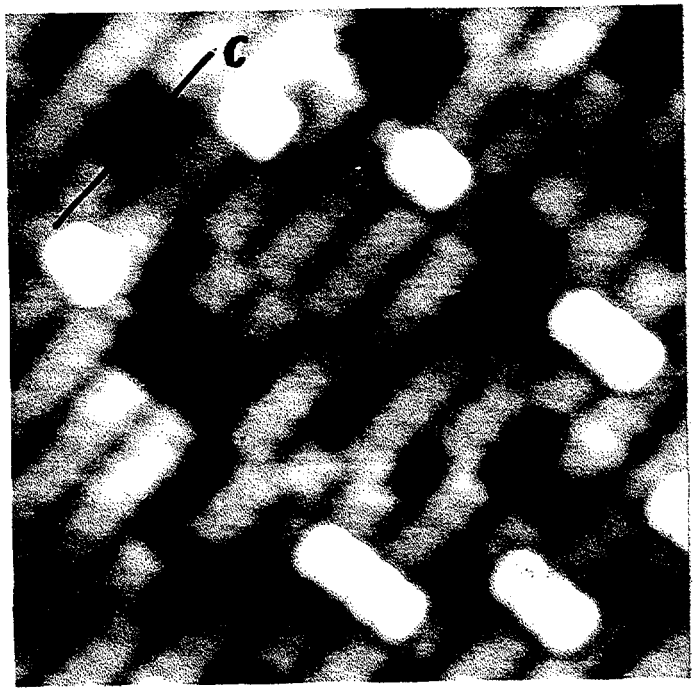

Figure 16. Si(100)-Sb STM image cross-section.[71] A cross section taken along C across one of the bare regions shows that the STM sees the step edge height of the overlayer to be 1.41 Å. This number will be compared to the SEXAFS results presented below to see if the electronic structure of the system affects the appearance of the overlayer.

atomic layer, a point of some controversy.[63,65–67] Therefore the chemical identity of the surface atoms should still be determined experimentally.

Despite these unresolved issues, the STM images provide a unique real-space view of the sample on an atomic scale. While it is impossible to extract an accurate bond length, one can identify the types and nature of defects in the overlayer. The two most obvious imperfections are bare regions of Si, and some second-layer occupation. The third, and by far the most interesting defect is the anti-phase boundary. As we can see in Fig. 15, there are regions of perfect 2x1 symmetry. But if we follow one of the dimer rows, we can arrive at a place where the dimers shift by one unit cell. Closer observation shows that these domains vary in size, but average about 40 Å across. This is significantly smaller than the coherence length of LEED, which is on the order of 150 Å. These small domains, that are out of phase with each other, explain the weak intensity of the second-order spots. Destructive interference diminished the spot intensities.

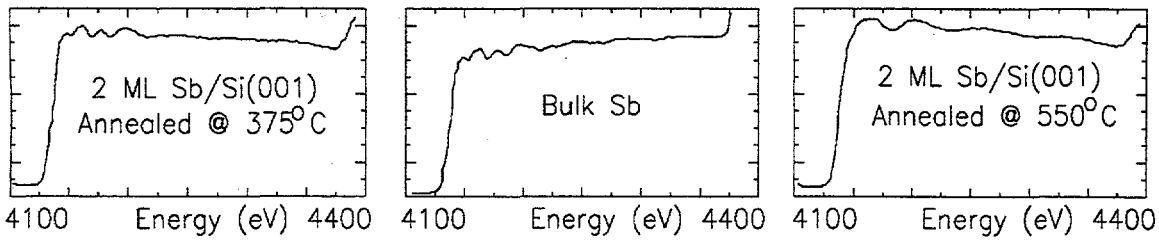

Figure 17. Sb L_3-edge EXAFS *vs.* anneal temperature. The three spectra of the Sb $L_3M_{4,5}M_{4,5}$ Auger electron yield demonstrate the effect of annealing two monolayers (ML) of Sb deposited on the Si(100) 2x1 surface. The top spectrum, that from 2 ML annealed at 375°C, is identical to the second plot, obtained from bulk Sb. The third spectrum was obtained from the same sample re-annealed at 550°C. The elimination of near-edge structure indicates a decrease in long-range coordination. The increase in period of the fundamental EXAFS oscillation indicates that the bonding is dominated by shorter bonds than pure Sb.

We can take a slice through one of the images. The cut is labelled C in Fig. 16. Here we can measure the height of overlayer. While we measure a step edge of 1.41 Å, we must keep in mind that this may not reflect the actual step height. The STM images only a small amount of the total charge density associated with the atom.[68] Because of this, electronic structure can, and does, affect the actual image obtained. But nonetheless, we will keep this number in mind to compare with the EXAFS results.

We have used the STM to determine the surface unit cell dimensions of the Sb-Si(100) surface. The STM images also explain the lack of intensity of the second-order spots on the LEED pattern obtained from the sample. Further, we have identified the nature of the defects inherent to the system: bare regions, second-layer occupation, and anti-phase boundaries. We suggest that the LEED intensities are explained by the size of the anti-phase boundaries, which are typically on the order of 40 Å across.

Our lack of success in imaging the samples prepared according to the recipe of Rich *et al.*[55], when combined with the quality of the images obtained from the samples annealed at higher temperatures suggest that 375°C is not a sufficient anneal temperature to form an unclustered, ordered Sb overlayer. The fact that the LEED

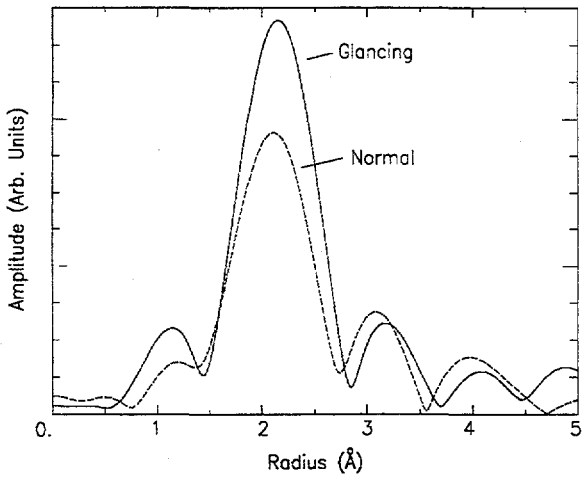

Figure 18. Angular dependence of the Sb L_3-edge EXAFS. Examination of the angular dependence of the EXAFS Fourier transforms gives information about bond directions. A best fit to the data assumes that the peak at 2.1 Å is due to Si backscattering and the peak at 3.2 Å is due to Sb backscattering. The decrease in amplitude of the peak at 2.1 Å as the incidence angle is varied from glancing to normal incidence indicates that the bond lies along the surface normal. In a similar way, we can see that the Sb-Sb bond at 3.2 Å lies perpendicular to the surface normal.

pattern is identical in both cases suggest that the excess Sb clusters, forming clumps, are much smaller than the coherence length of LEED.

While we can infer an adsorption site along with the chemical identity of the topmost atomic species, we will look to surface EXAFS to provide experimental confirmation of our assumptions. SEXAFS will also give us the actual bond lengths involved, along with chemically specific quantitative information about coordination.

3.4 Surface EXAFS

As discussed previously, K- or L_1-edge EXAFS exhibits the most polarization dependence, and therefore is the most simple type of EXAFS data to analyze and interpret. Unfortunately, the Jumbo monochromator is limited to 4850 eV. This is well below the Sb K edge, at 30.5 KeV, and it is also only about 150 eV above the L_1 edge, at 4698 eV. While 150 eV is enough to do near-edge studies, it is too limited a range to extract an accurate bond length. Despite the lack of quantitative data that one can obtain from the L_1-edge spectra, this limited range can be used for a

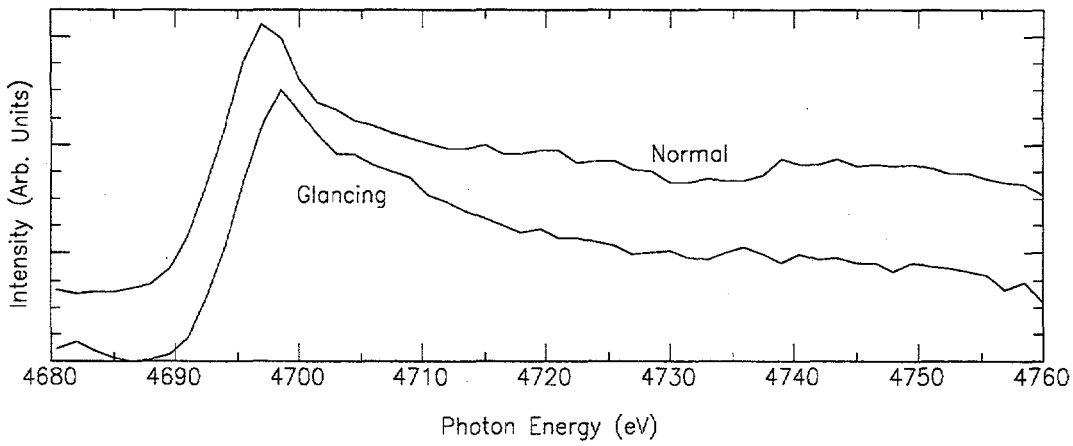

Figure 19. Angular dependence of the Sb L_1-edge EXAFS. While the Sb L_1-edge EXAFS could be collected for only 100 eV above the edge, this region includes the range that Sb backscattering amplitude is much greater than that of Si. Therefore the previously-discussed fingerprinting technique can be applied. The angular dependence of the feature at 4720 eV indicates that the Sb-Sb bond lies parallel to the surface.

qualitative indicator of bond direction, as will be discussed below. The L_2 edge rides on the L_3 EXAFS, making data analysis impossible. Therefore the Sb L_3 edge was used for our study.

Of the three available electron detection schemes, total yield, LMM Auger yield and MNN Auger yield, the LMM Auger yield was chosen. The LMM Auger signal exhibited the best combination of signal-to-noise and step-edge–to-background ratios. The Sb LMM Auger electron is at approximately 3017 eV. Therefore a bias voltage of 1175 V was applied to the sample in order to bring the Auger electron into the range of allowable energies for the CMA. The best counting rate was obtained in Auger mode. Since SEXAFS is a constant-final-state experiment, the resolution is determined by the monochromator. Therefore the decrease in analyzer resolution by using Auger mode as opposed to XPS did not pose a problem while increasing counting rates.

The first samples studied were annealed at 375°C. The Sb L_3-edge EXAFS spectra are shown in Fig. 17. The L_3-edge EXAFS from pure Sb is shown for comparison.

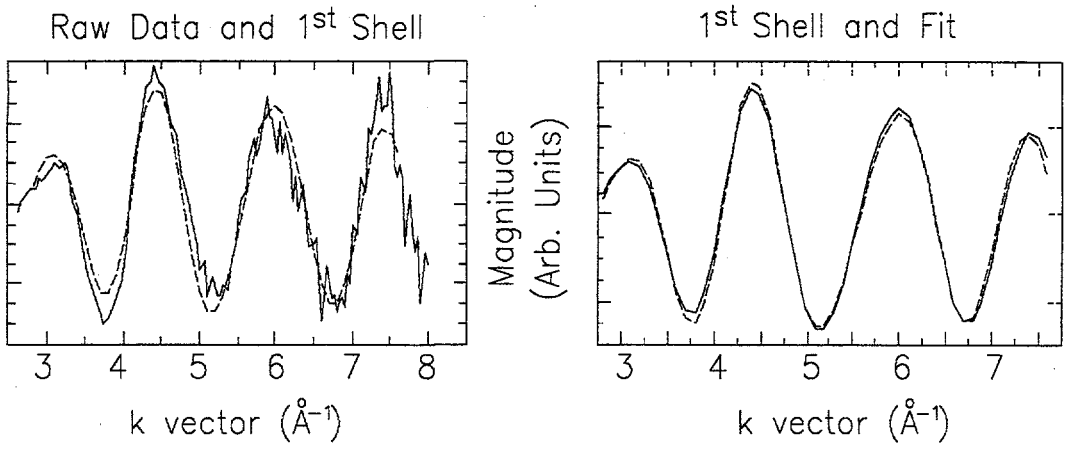

Figure 20. Sb-L_3 edge magic angle EXAFS: Raw data, 1^{st} shell contribution, and fit. A smooth window function was used to isolate the contributions to the Fourier transform of the k^2 weighted magic angle SEXAFS spectrum from Si and Sb nearest neighbors. This was then back transformed and a two-shell fit was applied. The raw data, back transform (dashed line), and fit are shown. The left figure shows that most of the signal is derived from the first shell, containing both Sb and Si. The figure on the right shows the accuracy of the fit. The Sb-Si bond length is 2.63 Åand the Sb-Sb bond length is 2.91 Å. Coordination numbers are presented in Table 3.

The similarities between the two spectra are obvious. This similarity is attributed to the presence of Sb clusters. Similar behavior has been observed on Ge,[69] as well as on several 3-5 semiconductors.[70] Since we obtained a two domain 2x1 LEED pattern from this sample, we infer that the Sb clumps are much smaller, 10 to 20 Å in size, than the coherence length of LEED, which is about 100 Å. Antimony is a much stronger backscatterer than is Si, so the presence of a relatively small amount of clusters dominates the SEXAFS spectra. After an anneal at 550°C, the SEXAFS spectra were no longer identical to that of bulk Sb. These results indicate that in some cases SEXAFS can be much more sensitive to the presence of small clusters than photoemission. We also observed a 20% decrease in the Sb Auger amplitude upon the 550°C anneal.

The evolution of the SEXAFS spectra as a function of anneal temperature is the first indication of the relative bond strengths of the Sb-Si bond as compared to the Sb-Sb bond. The Sb-Si bond must be significantly stronger than the Sb-Sb bond. If

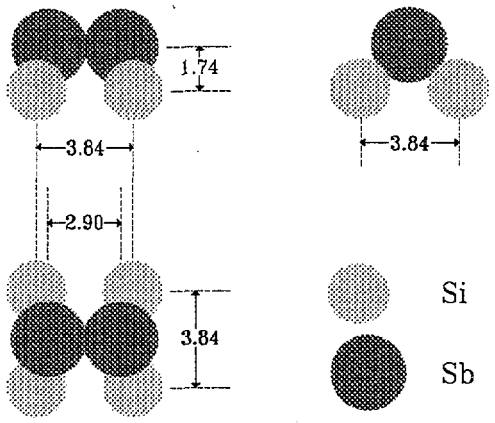

Figure 21. Geometry of the Sb-dimer model. A top and side view of the Sb dimer are shown along with the bond lengths extracted from the Sb L_3-edge magic-angle SEXAFS. Note that the dimer height of 1.74 Å as determined by EXAFS is 0.3 Å larger than the height as determined by STM. This is a concrete example of the types of effects that electronic structure can have on STM images.

this were not true, the Sb would dissociate from the Si before the Sb clusters desorbed. This is obviously not the case. This behavior has also been corroborated by others.[71]

The Fourier transforms of the grazing and normal incidence L_3 SEXAFS spectra obtained from a sample annealed at 550°C are shown in Fig. 18. The best fit to the data was obtained by assuming that the peak at 2.1 Å is caused by Si backscattering and that the peak at 3.2 Å is caused by Sb backscattering. The peak at 1.2 Å is due to truncation effects caused by the limited k-space range of data. The peak at 4 Å was not used in the data analysis; it corresponds to a combination of higher shells and truncation effects. The decrease in the peak amplitude at 2.1 Å as the incidence angle is varied from grazing to normal incidence is evidence that the Sb-Si bond has an appreciable component normal to the surface. The increase in the peak due to Sb-Sb bonding at 3.2 Å as the incidence angle is varied from grazing to normal incidence shows that the Sb-Sb bond is parallel to the surface plane.

The Sb backscattering amplitude is much larger than that for Si for low-k values; therefore the fingerprinting technique discussed in Chapter 2 can be applied. Because the Sb amplitude is so much larger than that for Si in this range, if we see any angular

effect in the EXAFS, we can attribute it to the Sb-Sb bond. Figure 19 shows both the grazing and normal-incidence Sb L_1-edge SEXAFS from the same sample as used for the L_3-edge measurements. The feature at 4720 eV that is present in the normal-incidence spectrum (upper spectrum) is not present in the grazing-incidence spectrum (lower spectrum). This implies that the Sb-Sb bond, the one we're fingerprinting, lies along the surface plane. This is in agreement with the conclusion obtained from the L_3-edge spectra, confirming our assumptions on the chemical identity of the two peaks previously identified in the Fourier transforms of the L_3-edge spectra. This effect is not as dramatic as in the Sb-Si(111) system due to the fact that each Sb atom bonds to only one other Sb atom on the Si(100) surface whereas each Sb bonds to two other Sb atoms on the Si(111) surface.

Incidence	Expt.	Fourfold Hollow	Bridge	Modified Bridge
Antimony-Silicon coordination				
Glancing	3.6 ± 0.4	2.97	2.50	2.41
Magic Angle	3.1 ± 0.4	3.99	2.52	2.70
Normal	2.5 ± 0.4	5.21	2.17	2.35
Normal/Glancing	0.7 ± 0.2	1.75	0.87	0.93
Antimony-Antimony coordination				
Glancing	0.7 ± 0.2	0.00	0.00	0.73
Magic Angle	1.1 ± 0.2	0.00	0.00	1.00
Normal	1.0 ± 0.2	0.00	0.00	1.20
Normal/Glancing	1.5 ± 0.2	– – –	– – –	1.53

Table 3. The effective $L_{2,3}$ coordination numbers as a function of angle. The effective coordination numbers are listed for several geometrical models along with the experimental values. The three adsorption models selected were chosen because, although two of the models do not contain Sb-Sb bonding, they make it possible to generate monolayer coverages that have no partially-filled dangling bonds on the surface. Partially-filled dangling bonds are unfavorable as they increase the surface energy. The modified bridge site model is supported by the SEXAFS experiment.

In order to extract the relevant bond lengths, a smooth window function was

used to isolate the contributions to the Fourier transform of the magic-angle SEXAFS spectrum from Si and Sb nearest neighbors. This was then back-transformed and a two-shell fit was applied. The raw data, back transform, and fit are shown in Fig. 20. The left graph shows that most of the signal is derived from the first shell, containing both Sb and Si. The graph on the right shows the accuracy of the fit. AlSb was used as the phase standard for the Sb-Si bond and bulk Sb was used as a standard for the Sb-Sb bond. The Sb-Si bond length was determined to be 2.63±0.03 Å. The measured value of 2.63 Å for the Sb-Si bond length is equal to the sum of the covalent radii of Si and Sb. The Sb-Si $L_{2,3}$ effective coordination number obtained at the magic angle is 3.1±0.4. The Sb-Sb bond length was determined to be 2.91±0.03 Å with an $L_{2,3}$ effective coordination number of 1.1±0.4. One must note that the $L_{2,3}$ effective coordination number is not as closely related to the absolute coordination number as in the K or L_1 edge case.[43] Therefore one must compare the measured values to theoretical models in order to determine the absolute coordination. The effective $L_{2,3}$ coordination numbers as a function of angle are listed in Table 3 for several geometric models along with the experimental values. The three adsorption models selected were chosen because, although two of the models do not contain Sb-Sb bonding, they make it possible to generate monolayer coverages that have a smaller number of partially-filled dangling bonds than the clean surface. Partially-filled dangling bonds are unfavorable as they increase the surface energy.[72,73] As demonstrated by Table 3, the modified bridge site model, shown in Fig. 21, is supported by the SEXAFS experiment.

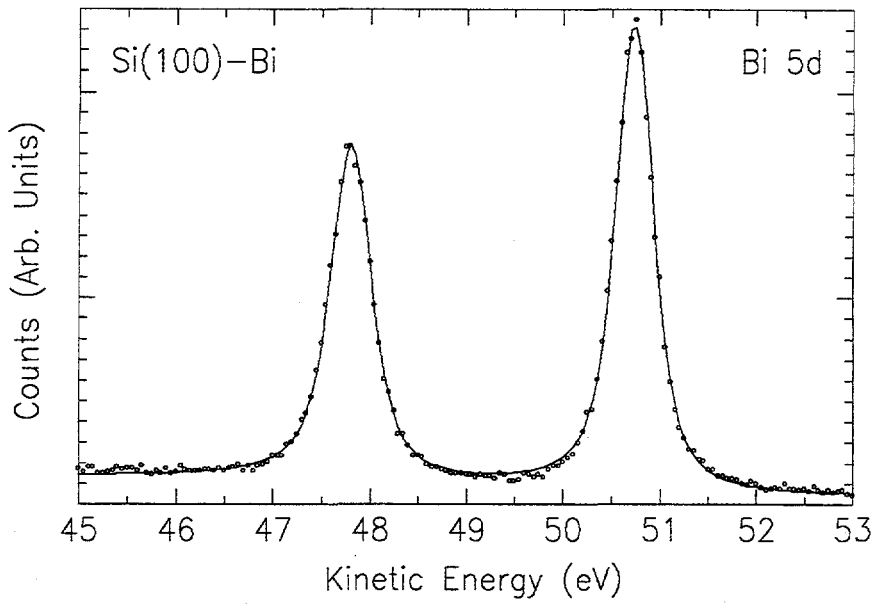

Figure 22. The Bi 5d core-level lineshape and fit. Bi 5d core-level data (dots), along with the fit (solid line) to the data, obtained with 80 eV photons are shown. A best fit was obtained using two singlet peaks at 47.83 and 50.76 eV. The Gaussian and Lorenzian widths were 0.28 eV and 0.32 eV for both peaks. The narrowness of the peaks indicates that Bi does occupy a unique site.

3.5 Photoemission Electron Spectroscopy

In order to correlate changes in the electronic structure to the evolution of the geometric structure as determined by STM and SEXAFS, we performed angle integrated core-level PES on both the clean and the Sb terminated surfaces. While this measurement had been performed before by others,[55] they observed that the Sb terminated surface had no interfacial component to the core-level lineshape. While it is true that Sb termination does narrow the core-level lineshape, we have found that an interfacial contribution still persists.

We increased the effective resolution of our experiment by obtaining the Si 2p core-level lineshape from the bismuth (Bi) terminated Si surface. Two ML of Bi were deposited on clean reconstructed Si(100). The sample was then annealed at 400°C for 5 minutes. This technique has been used by others to obtain single monolayer coverages of Bi on Si.[74] Figure 22 shows the Bi 5d core-level, along with the fits to

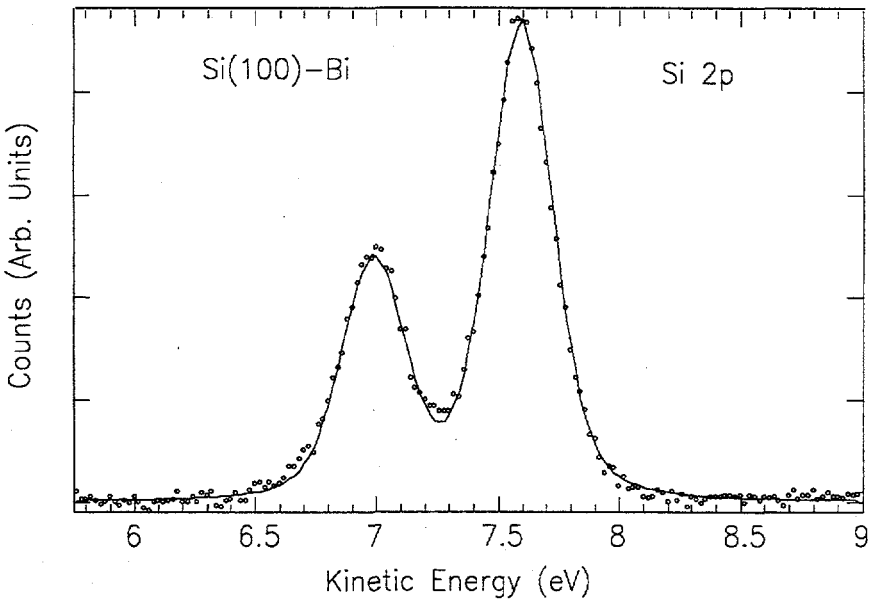

Figure 23. Si 2p core-level lineshape from the Si(100)-Bi surface. The Si 2p core-level spectrum obtained from the Bi terminated sample using 110 eV photons is shown along with the best fit. The elastic Si 2p photoelectrons have a kinetic energy of 7.5 eV and are relatively bulk sensitive. A best fit to the data was obtained using a spin orbit splitting of 0.61 eV, along with a Gaussian and Lorenzian width of 0.25 and 0.11 eV respectively. These parameters will be used to fit the Si 2p core-level lineshape obtained from the Sb-Si(100) system.

the data, obtained with 80 eV photons. A best fit was obtained using two singlet peaks at 47.83 eV and 50.76 eV. The Gaussian and Lorenzian widths were 0.28 eV and 0.32 eV for both peaks. The narrowness of the peaks supports our assumption that Bi does occupy a unique site.

Figure 23 shows the Si 2p core-level spectrum obtained from the Bi-terminated sample using 100 eV photons. The elastic Si 2p photoelectrons have a kinetic energy of 7.5 eV, giving them an escape depth of approximately 25 Å, and as such, are relatively bulk sensitive. A best fit to the data was obtained using a spin orbit splitting of 0.61 eV, along with a Gaussian and Lorenzian width of 0.25 eV and 0.11 eV respectively.

While it is true that the intrinsic Si 2p line width is smaller than we obtained experimentally, it cannot be larger. In fact, two independent groups[75,76] have recently used the combination of 2-ML epitaxial Ge overlayers and state-of-the-art beamlines

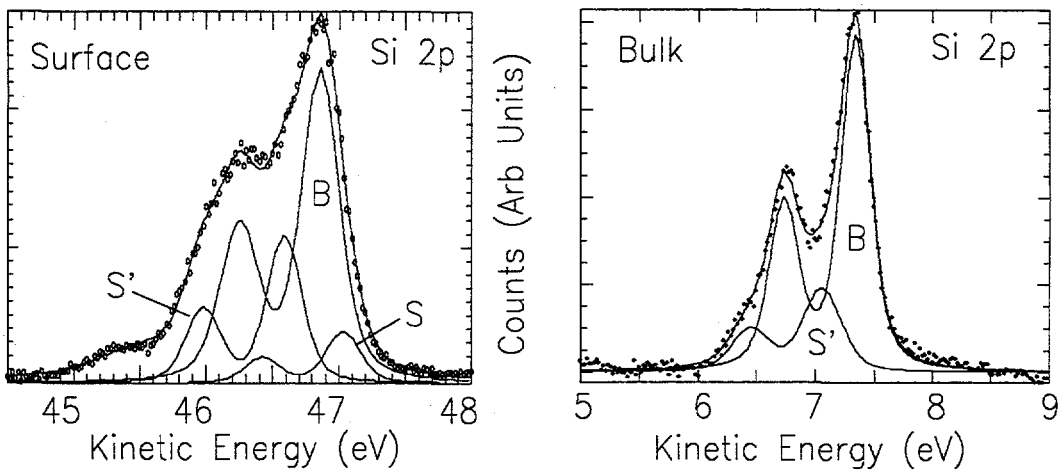

Figure 24. Si 2p core-level lineshape from the Si(100) 2x1 surface. The left spectrum, a surface sensitive Si 2p core-level, was obtained from the clean Si(100) 2x1 surface using 150 eV photons. The escape at 47 eV is approximately 5 Å. An integrated background has been removed. There is a small oxide peak present (on the low KE side), but comparison with other work has shown that its presence does not affect the conclusions drawn. The fits to the data are also shown. We have resolved three distinct peaks. The most intense of these, labeled B, originates in the bulk of the crystal. The two other peaks, S and S′, come from the Si atoms forming the surface dimers and the 2^{nd} Si layer. Fits to the data show that Peak S is 0.21 eV higher in binding energy relative to the bulk peak while peak S′ is 0.27 eV lower in binding energy than the bulk peak.

to obtain even narrower intrinsic line widths.

Figure 24 shows the surface-sensitive Si 2p core-level spectrum obtained from the clean Si(100) 2x1 surface using 150 eV photons. The escape depth at 47 eV is approximately 5 Å. An integrated background has been removed. There is a small oxide peak present, but comparison with other work has shown that its presence does not affect the conclusions drawn.

The fit to the data is also shown in Fig 24. We have resolved three distinct peaks. The most intense of these, labeled B, originates in the bulk of the crystal. The two other peaks, S and S′, come from the Si atoms forming the surface dimers and the second Si layer. Fits to the data show that Peak S is 0.21 eV higher in binding energy relative to the bulk peak while peak S′ is 0.27 eV lower in binding energy than the bulk peak. Figure 25 shows a perspective view of the Si(100) 2x1 surface along with the corresponding core-level component assignments.

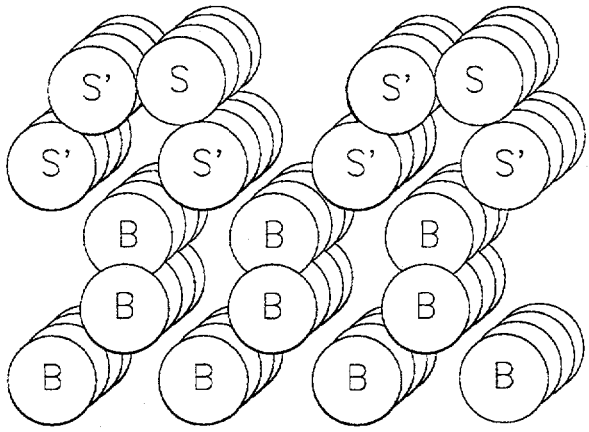

Figure 25. Atomic assignments of the Si 2p core-level components. The three resolved components of the Si 2p lineshape from the clean Si(100) surface correspond to particular Si atoms. A pespective view is shown. The peak labelled B is associated with Si atoms three or more layers deep. The peak labelled S is associated with the second Si layer and one of the atoms forming the dimer. The peak labelled S$\prime$ is associated with the remaining Si dimer atom.

Upon Sb deposition and annealing, the Si 2p lineshape changes drastically (Fig. 26). The peak S at 47.03 eV in Fig. 24, disappears completely, leaving one interfacial core-level component, at -0.22 eV relative to the bulk component, labelled I in Fig. 25. We interpret the data in the following manner: Peak S is associated with the surface Si dimers. Its suppression is associated with the elimination of the Si dimer. The topmost Si layer is now associated with peak I. This is justified in that the topmost Si layer is now tetrahedrally coordinated like the second layer of the clean Si(100), which also has a peak, labelled S$'$ in Fig. 24, at nearly the same relative binding energy associated with it. The bulk peak originates from the second Si layer and deeper. Figure 25 also shows a perspective view of the Si(100)-Sb 2x1 surface along with the corresponding core-level component assignments.

To summarize, the evolution of the electronic structure of the Si(100) 2x1 surface as determined by our photoemission data is as follows: The Si 2p core-level lineshape is composed of at least three components. The peaks labelled S$'$ and S in Fig. 24 are associated with the topmost and second Si layers. The rest of the crystal is comprised of atoms with bulk-like electronic properties. The formation of

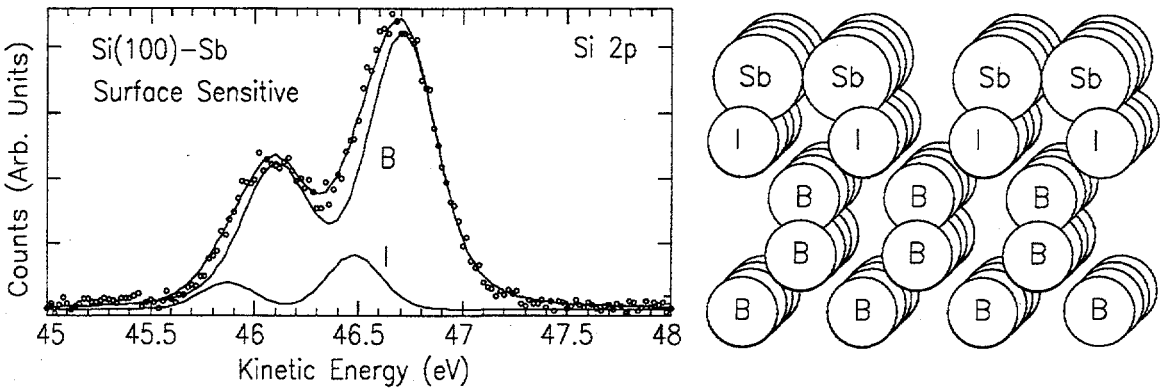

Figure 26. Si 2p core-level lineshape from the Si(100)-Sb surface. The peak S in Fig. 24 is eliminated by the formation of the Sb overlayer. Like the clean surface, the peak labelled B is associated with the bulk of the sample, the third and deeper atomic layer. In this case, this corresponds to the 2^{nd} Si layer. The peak labelled I is associated with the topmost Si layer. The peak position of I is -0.22 eV below the bulk position and corresponds to the peak labelled S′ in the lineshapes obtained from the clean sample. The corresponding atomic peak assignments are shown on the right.

an ordered Sb overlayer removes the peak associated with the Si dimers. Here we must note that angle-integrated photoemission itself cannot determine whether the Sb forms dimers. That information can be determined only by a structural probe such as LEED, STM or SEXAFS. Nonetheless, the PES results are consistent with and support the interpretation of both the STM and SEXAFS results.

3.6 Discussion and Conclusions

We have combined STM, SEXAFS, PES and LEED to provide a complete description of both the electronic and geometric structure of the Sb-Si(100) 2x1 system. By combining these techniques, we have obtained a complete description of both the short- and mid-range order of the system. STM has also provided us with the identity and nature of the defects inherent to this interface. The use of PES has allowed us to correlate the changes in electronic structure upon Sb adsorption to specific changes in the geometric structure.

The evolution of the SEXAFS spectra as a function of anneal temperature is also correlated to the geometric structure of the system. Upon deposition of more

than one ML of Sb and subsequent light anneals, the Sb forms an ordered overlayer of Sb dimers. The excess Sb forms small clumps that desorb completely by 550°C. The formation of Sb dimers accompanies the elimination of Si dimers, allowing the topmost Si layer to be four-fold coordinated. We have further correlated this change in geometric structure with the elimination of one of the surface contributions to the overall Si 2p core-level lineshape obtained from the clean Si(100) surface.

SEXAFS determined that the Si-Sb and Sb-Sb bonds in the Sb dimer are covalent in nature, with the bond lengths simply given by the sum of the covalent radii of the atoms, within experimental accuracy. The lengths obtained are 2.36±0.03 Å for Si-Sb and 2.91±0.03 Å for Sb-Sb. The absolute and relative $L_{2,3}$ coordination numbers also support the Sb-dimer model.

Our PES results are consistent with both the STM and the Surface EXAFS results. We have succeeded in resolving an interfacial component of the Si 2p core-level in the Sb-Si(100) interface by employing the use of a Bi overlayer to terminate the Si crystal. It is true that the existence of an interfacial component in the Si 2p core-level lineshape raises some questions about the assumptions used in the SEXAFS data analysis. Specifically, our assumption that the topmost Si atoms lie in an ideal bulk-like position may not be true. Calculation shows that it would take an unusually large displacement of the Si atoms to change the adsorption site as determined by SEXAFS.

Our results indicate that the Sb-Si(100) and the Sb-Si(111) system behave very similarly. Both systems exhibit the same clustering behavior. Upon Sb deposition and annealing at 550°C, Sb terminates both surfaces allowing the topmost Si atoms to regain their tetrahedral coordination. Both systems' bonds are covalent in nature, with the Si-Sb and Sb-Sb bonds being the same length in both systems, within experimental errors. Both these geometries allow the partially-filled dangling bonds of

the clean crystal to become filled, resulting in a much smaller surface free energy, and a relatively passivated surface.

The As-Si(100) systems behave similarly. The As bonds covalently to the Si(100) surface, forming dimers while eliminating Si dimers.[59] The most notable differences are that the coherent domains of 2x1 periodicity are much larger and the percentage of the surface covered by defects is much lower, as can be seen in the STM work of Becker *et al.*[60] Because As is one row above Sb in the periodic table, and has a correspondingly smaller atomic radius, I hypothesize that the density of interfacial defects in the Sb overlayer are stress-induced; that is to say, the Sb atoms are just a little too large to fit on the Si lattice, without the presence of strain-relieving defects.

We have also determined that the starting point for surfactant assisted Ge epitaxial growth on Si(100) is a Si(100) substrate terminated with Sb dimers. Charge neutrality requires that the Sb atoms each have one filled dangling bond, resulting in a very passivated surface. The large size of Sb atoms relative to Si atoms suggests that there will always be an appreciable defect density in the overlayer. While the role of these defects, if any, remains unclear, it is certain that some of the impinging Ge will "see" some bare Si. I must also point out that the kinetics of the Sb migration and the formation of an epitaxial Ge overlayer are still unclear. While a complete description of all the processes involved is beyond the scope of this thesis, another piece in the puzzle can be obtained by examining the Sb-Ge(100) system, the subject of the next chapter.

4. The Ge(100)-2x1 Sb Interface

4.1 Introduction

In the last chapter, we examined the Si(100)2x1-Sb interface in intimate detail. There were many motivating considerations, all of which also apply to the Ge(100)-2x1 Sb system. These ranged from the fundamental questions about the nature of surfaces and interfaces to investigation of what specifically about Sb, Si and Ge allows one to employ a modified growth mechanism to create interfaces that were previously impossible. In a way this chapter is a mirror image of the previous one. In Chapter 3, we employed a multi-technique approach to investigate how the presence of Sb modified the geometric and electronic structures of the Si(100) 2x1 surface in order to understand their correlation. In this chapter we investigate how the presence of Sb modifies the geometric and electronic structure of the Ge(100) 2x1 surface with the same goals in mind.

This study, however, employs fewer techniques than the Sb-Si work. This does not mean that a unique description is unattainable. We will once again employ a multi-technique approach to solving the surface structure. We will also correlate these changes to observed changes in the Ge 3d core-level lineshape. But we will be in a situation where more information must be extracted from each technique used. While we do arrive at a conclusion that is consistent with all the available data, we arrive there in a somewhat less dramatic fashion than in the previous chapter.

The ideal Ge(100) surface is known to form a dimerized 2x1 surface reconstruction.[77,78] The geometry of a dimer is shown in Fig. 27. In the same manner as for Si, this 2x1 surface reconstruction results in a factor-of-two decrease in the number of surface dangling bonds. But unlike Si, the Ge(100) 2x1 reconstruction is comprised of asymmetric dimers. The Ge-Ge dimer bond is rotated 17° out of plane. This dimer

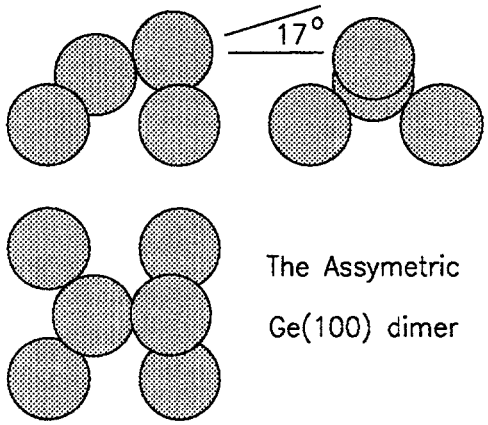

Figure 27. The Ge(100) 2x1 surface reconstruction. The reconstruction is similar to that of Si(100) 2x1 surface. It is comprised of individual dimers like the one shown. Unlike the essentially symmetric Si dimer, the Ge dimer is asymmetric, with the Ge-Ge dimer bond forming an angle of 17° with the (100) surface. This reconstruction results in and is driven by a factor-of-two decrease in the number of surface dangling bonds. The charge transfer that accompanies the dimer buckling further reduces the surface energy.

relaxation results in charge transfer from one of the partially-filled dangling bonds to the other, resulting in a net decrease of the effective number of partially-filled dangling bonds on the surface.[72,73]

While the Ge(100) 2x1 surface reconstruction shares both geometry, with the exception of dimer buckling angle, and electron counting behavior as the Si(100) 2x1 surface, the Ge lattice is almost 7% larger. In Chapter 3, we saw that the Sb dimer is a little too large to form a perfect overlayer. It is possible that the Sb-Ge system could be more ideal. With all the similarities between Ge and Si, one might naturally expect the Sb-Ge(100) interface to be similar to the Sb-Si(100) interface, and indeed, this is what is found.

LEED shows that the Sb overlayer has a 2x1 symmetry. The LEED pattern is similar to that obtained from the Sb-Si(100) surface, a bright 1x1 pattern with diffuse two-domain 2x1 pattern superimposed. This may indicate the presence of coherent domains separated by anti-phase boundaries, but due to the lack of STM images, this is just conjecture. LEED patterns from vicinal Ge(100) also show that the symmetry

direction rotates by 90°, indicating that the 2x1 symmetry after Sb deposition is due to a new layer on the surface, and not a replacement reaction.

Core-level PES shows that the Ge 3d lineshape from the Ge(100)2x1 and Sb-Ge(100) behaves in a fashion similar to the Si 2p core-level lineshape in the Sb-Si(100) system. Using conventional curve-fitting techniques, three components are found to contribute to the overall lineshape obtained from the clean, reconstructed surface. These two peaks are at 0.21 eV and 0.51 eV higher kinetic energy relative to the bulk peak. Upon Sb deposition and a 400°C anneal, the Ge 3d surface component with the highest kinetic energy is eliminated, leaving only one interfacial componant at 0.21 eV higher kinetic energy relative to the bulk contribution. This is interpreted as the result of the elimination of Ge dimers, as was the case in the Sb-Si(100) system. PES intensities indicate that the Sb resides on the surface.

SEXAFS spectroscopy was used to determine both the first-shell distances and the interfacial behavior as a function of anneal temperature. The presence of excessive amounts of Bragg peaks in the SEXAFS spectra allowed for the collection of data only near the magic angle, 54.7°.[63] Because of this, only bond lengths could be obtained. The spectra could be fit only by including both Sb-Sb and Sb-Ge bonding. This, combined with the nearly covalent bond lengths obtained, indicates that the Sb forms dimers on the Ge(100) surface. Once again, the system behaves in a fashion similar to the Sb-Si(100) system.

Although all the properties discussed so far are exactly the same as for the Sb-Si(100) system, the evolution of the SEXAFS spectra from the Sb-Ge system as a function of anneal temperature differs from that of the Sb-Si system. It appears that the desorption of Sb from the Sb-Ge(100) system proceeds smoothly, without a range of temperatures over which the excess Sb has desorbed, leaving only a single ordered monolayer. All excess Sb desorbs from the Si(100) surface at less than 450°C,

leaving a single dimerized monolayer of Sb. This layer is stable to temperatures of at least 550°C before all Sb desorbs completely at 600°C. In the case of the Sb-Ge(100) system, SEXAFS indicates that while a 350°C anneal is capable of ordering the system, it is insufficient to desorb the excess Sb. At temperatures sufficient to completely desorb the excess Sb, it appears that the underlying Sb monolayer is already starting to desorb. There is, however, a small range of temperatures very near the desorption temperature for which a stable interface exists that is comprised of less than one monolayer of Sb involving only Sb-Ge bonding. Unfortunately, the SEXAFS amplitude is very low. This fact combined with the inherent difficulty in analyzing L_{23}-edge EXAFS, renders the spectra obtained from this system impossible to analyze quantitatively with any degree of confidence.

Despite the limitations of the SEXAFS data, we still have come to a complete description of the Sb-Ge(100) interface. Although we cannot independently identify the nature of the overlayer defects, we can infer that they are of the same type as those present in the Sb-Si(100) system, although their relative and absolute densities may be rather different. These results and their implications on the behavior of Sb as a surfactant will be critically examined in the conclusion of this thesis, in the next chapter.

4.2 Experiment

The Ge wafer samples were initially degassed for six hours at 600°C. The Ge was then sputtered with 500 eV Ar ions arriving at an angle of 45° to the surface. The resulting ion damage was removed by annealing the sample at 800°C for 10 minutes. It was found that higher-energy ions or more normal incidence resulted in excessive sample disorder that annealing could not remove. All temperatures were measured with a thermocouple attached to the manipulator head. Pressures during the sample

heating did not exceed $1.0x10^{-9}$ torr. A sharp two-domain 2x1 LEED pattern was observed. For both the PES and the SEXAFS measurements, two ML of Sb were deposited onto a substrate at room temperature at a rate of 2 ML per minute and subsequently annealed at 375°C for 15 minutes. During deposition and annealing, the chamber pressure was held below $1x10^{-9}$ torr. LEED showed a 1x1 pattern with diffuse two-domain 2x1 spots. LEED was also performed on vicinal Ge(100), cut 4° off axis. This single-domain Ge was characterized by a single-domain 2x1 LEED pattern.[79]

The PES spectra were obtained on beamline 3-1, the New Grasshopper,[38] at SSRL, using the same chamber as was used for the SEXAFS study and most of the Sb-Si work. PES of the clean surface could not detect the presence of any contaminants. Conventional data reduction and fitting techniques were used to analyze the PES spectra. While use of the overlayer technique as described in Chapter 2 and used in Chapter 3 was attempted, it turns out that the Ge 3d bulk-sensitive lineshape from the Bi-Ge(100) system is of comparable width to that derived from the Sb-Ge system.

The SEXAFS data were recorded using the JUMBO double crystal monochromator[61] at SSRL. The energy resolution of this monochromator is 1.9 eV at a photon energy of 4100 eV using Ge(111) crystals. The experimental chamber (base pressure better than $7x10^{-11}$ torr) consists of a main chamber housing LEED optics, a load lock system, and a double-pass cylindrical mirror analyzer (CMA), the axis of which lies along the polarization vector of the synchrotron radiation. The sample manipulator has an on-axis configuration that allows the sample normal to rotate in the plane formed by the CMA axis and the direction of light propagation. Samples were prepared in an adjacent chamber equipped with an electron beam heater, Sb sources, ion gun and a quartz-crystal rate monitor. The samples were moved between the main chamber, the preparation chamber and the load lock system with magnetically

coupled transfer arms.

The Sb L_3 edge SEXAFS were collected by monitoring the Sb MNN Auger emission as a function of incident photon energy and flux in the constant final state mode[62] as well as by monitoring total yield. The Sb LMM Auger electron could not be used for data collection due to a Ge core-level sweeping through the relevant energy window. Because of the presence of Bragg peaks in the SEXAFS spectra, data could be collected only near the magic angle. While this does make bond direction assignments impossible based on SEXAFS amplitudes, we can still determine the nearest-neighbor distances and chemical identity.

SEXAFS spectra were collected over a large range of anneal temperatures, ranging from 375°C to 600°C, in order to investigate the possibility of Sb clumping, as previously observed in the Sb-Si system.

4.3 Low-Energy Electron Diffraction

Due to the lack of STM images, we will examine the LEED behavior of the Sb-Ge(100) interface in somewhat greater detail. The clean reconstructed Ge(100) surface is comprised of Ge dimers. Since the size of individual coherent domains is much smaller than the sample area sampled by the electron beam, multiple domains contribute to the LEED pattern. This results in a two-domain 2x1, or 2x2 pattern. In order to eliminate the effects of multiple domains, vicinal (4° off ideal) Ge(100) was used for some of the LEED studies. The clean reconstructed vicinal Ge(100) is characterized by a single-domain 2x1 pattern. This is due to the energetic favorability of double steps over single steps.[79]

The first sample examined was a Sb-Ge(100) sample annealed at 400°C for 10 minutes. While the LEED pattern remained a 2x2/2-domain 2x1 pattern like that

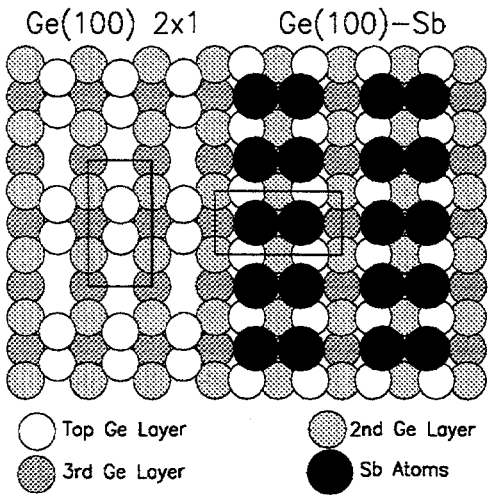

Figure 28. The Sb-covered and clean Ge(100) surface. The Sb dimers are rotated by 90° relative to the original Ge surface dimers. The formation of an overlayer of Sb dimers results in a rotation of the LEED pattern by 90°. A rectangular box shows the surface unit cell of both the clean and Sb-covered surfaces.

obtained from the clean Ge surface, only the 1x1 spots remained sharp. The higher-order spots became blurred and somewhat dimmer. While this could be interpreted as a poorly-ordered surface, I choose to interpret it as the result of the presence of antiphase boundries, in analogy with the Sb-Si(100) system. Unfortunately, LEED from flat Ge(100) samples cannot determine if the pattern is 2x2 or a two-domain 2x1. In either case, anti-phase boundaries can occur, which would account for the diffuseness of the higher-order spots. The LEED behavior is similar from all samples regardless of anneal temperature. Above 600°, the LEED pattern sharpens considerably, consistent with the desorption of all of the Sb. Once again, our conclusions are supported by the analogous behavior of the Si(100)-Sb surface.

The LEED behavior of the vicinal surface is much more revealing. As previously mentioned, the LEED pattern obtained from the vicinal Ge(100) is a single-domain 2x1 pattern. Upon Sb deposition and annealing, the pattern rotates by 90°. If we assume that Sb resides on the surface of the Ge, we infer that the Ge dimer bond is broken. If it were not, the LEED pattern wouldn't rotate. This would further imply

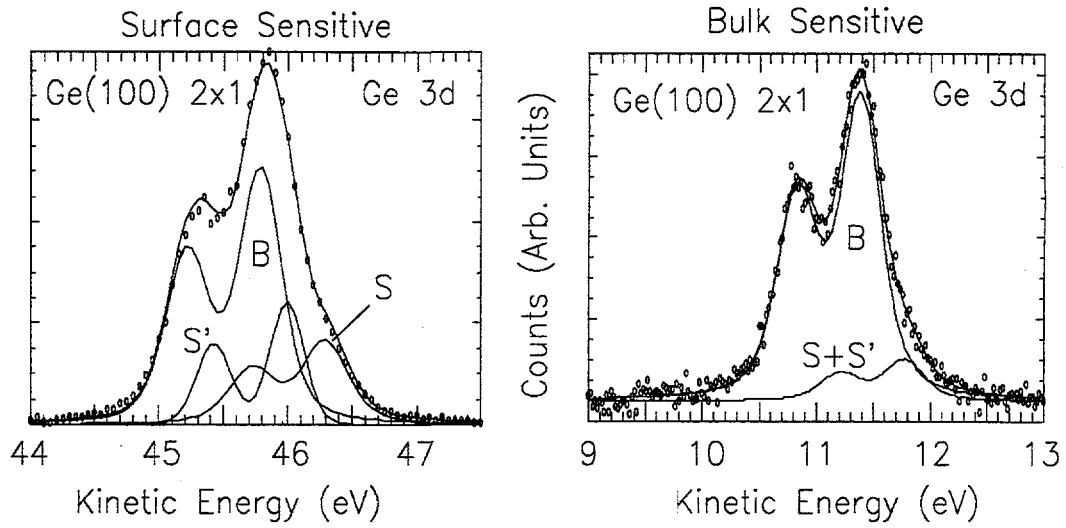

Figure 29. The Ge 3d core-level lineshape from the Ge(100) 2x1 surface. The data, fit and deconvolution are shown for both the surface- and bulk-sensitive kinetic energies. In the surface-sensitive spectrum, three components are resolved. The peak **B** originates in the bulk of the sample, three and greater atomic layers deep. The other two contributions, **S**, and **S'** are associated with the top two atomic layers. The parameters extracted from the Ge(100)-Sb bulk-sensitive Ge 3d spectrum were used for fitting the data. The bulk-sensitive spectrum is included for completeness.

that the Sb formed dimers, but with the symmetry direction rotated 90° from that of the original Ge dimers, resulting in the 2x1 symmetry observed by LEED. Figure 28 shows top views of both the clean and Sb-covered Ge(100) 2x1 surfaces.

The LEED data are consistent with the formation of an overlayer of Sb dimers on an unreconstructed Ge(100) surface. The diffuse nature of the higher-order spots would indicate the presence of anti-phase boundaries between coherent domains whose size is still less than the coherence length of LEED. This sets the upper limit on the size of the coherent domain at approximately 100 Å.

Based on the Sb dimer model, we expect the following: The PES behavior should be similar to that of the Sb-Si(100) system and the bonding should be fairly covalent, with both Sb-Sb and Sb-Ge bonding observable in the SEXAFS spectra. We will examine these issues in the next two sections.

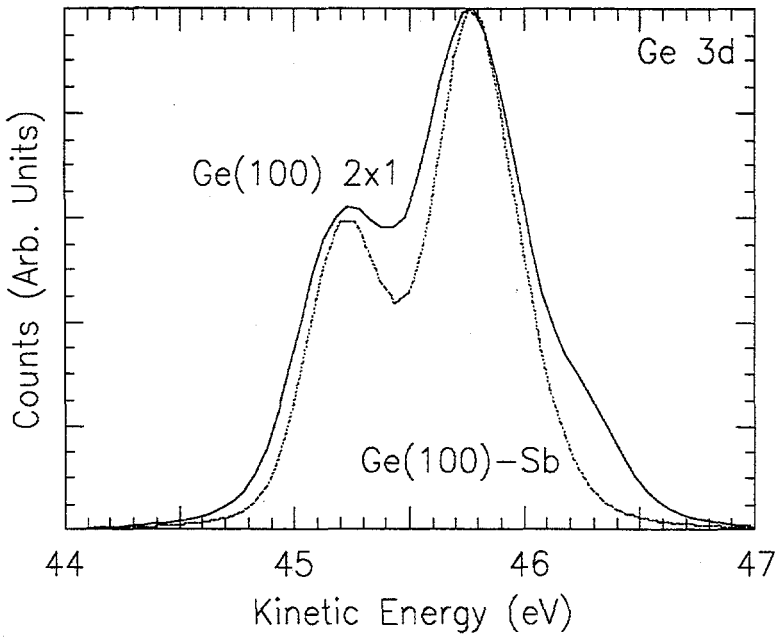

Figure 30. The Ge 3d core-level lineshape from both the clean and the Sb-terminated Ge(100) surface. Both peaks have been scaled in order to emphasize the narrowing of the lineshape upon Sb termination of the surface. The narrowing of the lineshape is consistent with and supports the conclusion that the Sb termination results in the elimination of the Ge(100) surface dimers.

4.4 Photoemission Spectroscopy

As previously mentioned, the clean, reconstructed Ge(100) 2x1 surface is comprised of dimers. Therefore we should expect the Ge 3d core-level lineshape to be fairly similar to the Si 2p from the Si(100)2x1 surface. Figure 29 shows both the total Ge 3d core-level lineshape after background subtraction, along with the final deconvolution into three peaks. The largest peak, labeled B, is associated with the atoms three and more atomic layers deep, while the remaining two peaks are associated with the top two atomic layers. Upon Sb termination, one of the surface contributions, that associated with the Ge dimers, is eliminated. This result in itself demonstrates that the Ge dimer bonds have been broken. Figure 29 shows the surface-sensitive Ge 3d core-level lineshape obtained from the Sb terminated surface with the spectrum from the clean surface superimposed. The two peaks have been scaled to accentuate the lineshape narrowing upon Sb adsorption. Figure 30 shows both the total core-level

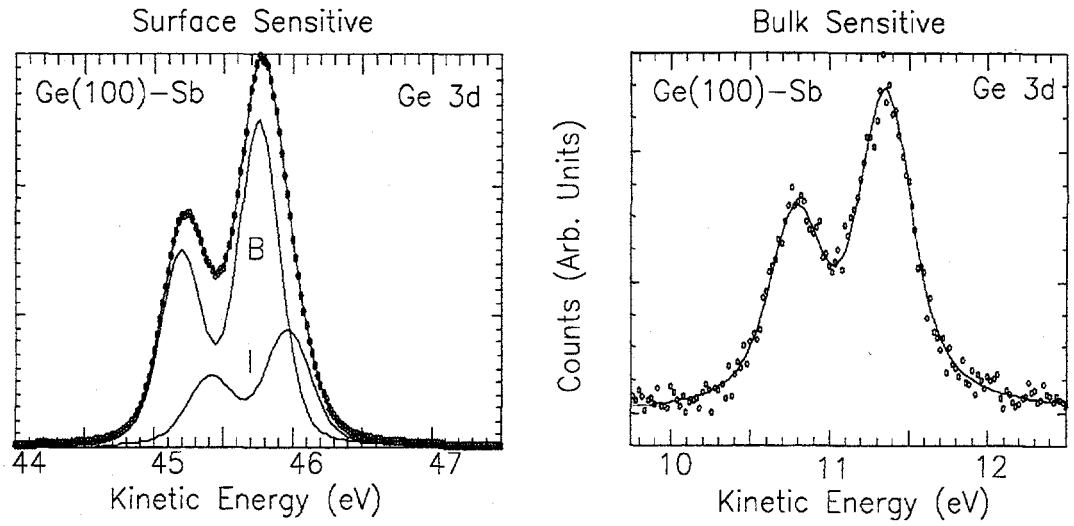

Figure 31. The Ge 3d core-level lineshape from the Ge(100)-Sb surface. The data, fit and deconvolutions for both the bulk and surface-sensitive spectra are shown. Because it was found that the Ge 3d core-level lineshape derived from the Ge(100)-Bi surface is of comparable width to that obtained from the bulk-sensitive spectrum above, conventional techniques were used to deconvolve the data.

lineshape and the deconvolution into two peaks.

In the Sb-Si(100) system, we saw that this change in electronic structure was associated with the elimination of Si dimers, supporting our assertion that the Ge dimers have been supressed. We can examine the spectra further to learn more. The key assumption that led to the postulation of the Sb dimer model based on the LEED data was that the Sb lies on top of the Ge. This is confirmed by the change in photoemission intensities. Several recent works[6–8,81] also show that Sb will migrate to the surface upon annealing if the Sb overlayer has Ge deposited on top of it. Upon deposition of Ge onto the overlayer, the Sb intensity decreases. When the sample is then annealed, the Sb amplitude returns to its original amplitude, thus comfirming the assumptions made in the interpretation of the LEED behavior of the vicinal surface.

4.5 SEXAFS

A study of the SEXAFS amplitudes as a function of angle was not possible due to the presence of Bragg peaks in the spectra. Only a small range of angles near the Magic Angle did not show any Bragg peaks in the energy range of interest. At first, this may seem to eliminate SEXAFS as a useful probe on this system. If SEXAFS alone were used, this indeed would be the case. We can learn something about the system nonetheless because of the constraints on the system imposed by both the LEED and PES data.

We know that the Sb resides on top of an unreconstructed Ge(100) surface. The behavior of the Ge 3d core-level lineshape indicates that the presence of the Sb overlayer removes the Ge dimer bond. We further know that the Sb forms a 2x1 LEED pattern that is rotated by 90° relative to the Ge(100) 2x1 LEED pattern. These three facts alone strongly indicate that the Sb is forming dimers on the Ge(100) surface. This behavior, analogous to the Sb-Si(100) system, would predict that the bond lengths involved are nearly covalent.

Analysis of the Sb L_3-edge EXAFS spectrum does indeed confirm that the bonding involved is covalent. Spectra were collected as a function of anneal temperature. Figure 32 shows the evolution of the SEXAFS spectra as the anneal temperature is increased. A continuous decrease in the SEXAFS edge height indicates there is no temperature range over which excess Sb is desorbed while the underlying Sb dimer layer remains intact. Because of this, bond lengths were extracted from one of the spectra that still exhibited a slight amount of clustering. While this does result in skewed coordination numbers, we still can measure accurate bond lengths for both the Sb-Ge and Sb-Sb bonds. For more heavily reacting systems, this would not be allowed because the Sb-Sb bond length will be weighted towards the bulk value. For

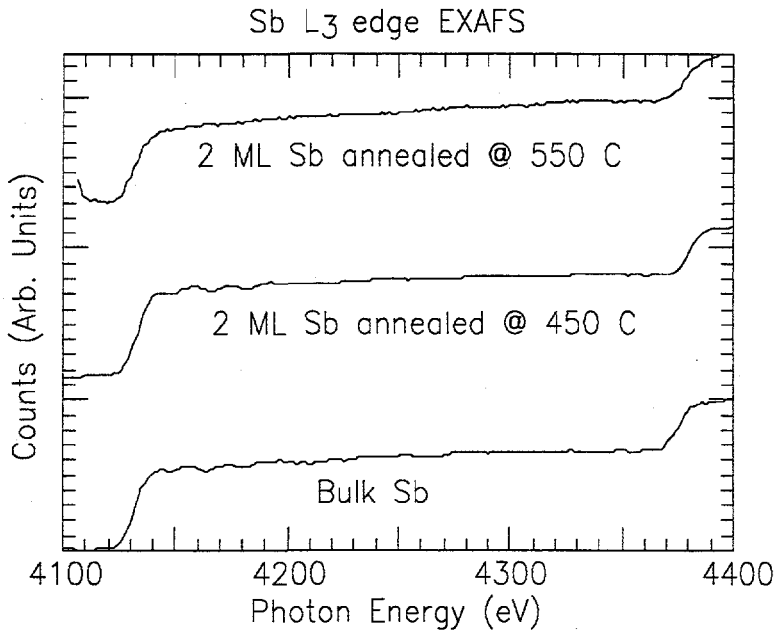

Figure 32. The Sb L_3-edge magic angle EXAFS *vs.* anneal temperature. The upper spectrum, from the sample annealed at 550°C, shows 15% of the edge jump of the middle spectrum, consistent with the desorption of Sb. Unfortunately, this spectrum proved to have insufficient amplitude for reliable analysis. The spectrum obtained from the sample annealed at 450°C still shows the near-edge structure characteristic of clustered surfaces. All evidence of clustering on the Si(100)-Sb surface is gone by this anneal temperature. We found no temperature that resulted in the desorption of all excess Sb, while leaving an intact Sb-terminated Ge(100) surface. This indicates that the Sb-Ge bond is not as strong as the Sb-Si bond. The bulk Sb L_3-edge EXAFS spectrum is included for comparison.

this system, this is not expected to affect the results because the Sb-Sb bond in the Sb-Si(100)2x1 system is found to be equal to the bulk value within experimental error. The Sb-Sb bond length in the Ge(100)-Sb surface has recently been measured to be 2.91±0.03Å by X-ray diffraction,[80] in agreement with our assumptions and results. While all these constraints on the SEXAFS data, along with the difficulties inherent to $L_{2,3}$-edge EXAFS analysis,[43] do not make analysis impossible, they do result in unusually large error bars of ±0.06 Å as opposed to the typical value of ±0.03 Å.

Figure 33 shows the EXAFS spectrum and the first-shell contribution along with the fit to the data. The best fit to the data indicates that the Sb-Sb bond length is 2.91 ± 0.06 Å and that the Sb-Ge bond length is 2.58 ± 0.06 Å. These values are close to the sum of covalent radii within the experimental error indicating that the bonds

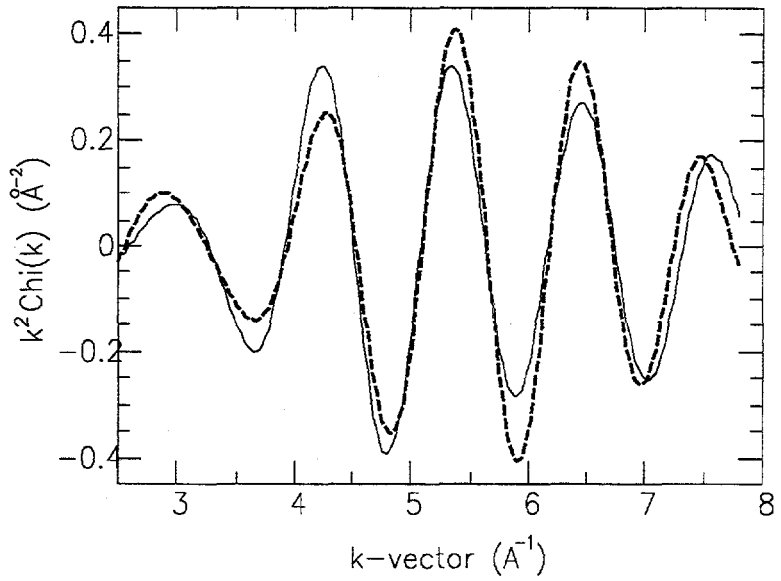

Figure 33. The Sb L_3-edge Magic-Angle EXAFS spectrum: Raw data, 1^{st} shell contribution, and fit. The spectrum from the 450°C anneal sample was used for bond length determination. The presence of some residual Sb clusters preclude the possibility of accurate coordination number extraction. The bond lengths, as determined by EXAFS spectroscopy, are 2.91 ± 0.06 Å and 2.58 ± 0.06 Å for the Sb-Sb and Sb-Ge bonds, respectivly.

are nearly covalent, as predicted by the Sb dimer model of the surface.

4.6 Discussion and Conclusions

Once again we have used a multiple-technique approach to determine the geometric structure of an experimentally difficult system. We have further provided information on the correlation of the changes in geometric and electronic structure. We have shown that the Ge(100)2x1-Sb surface is described by the Sb dimer model. While one could argue that in the case of the Sb-Si(100) system discussed in Chapter 3 the overlayer structure could be determined using only SEXAFS or STM, this is not the case for the Sb-Ge(100) system. None of the techniques by itself results in a complete enough data set successfully to determine the overlayer geometry. LEED patterns indicate only that the 2x1 reconstruction is rotated relative to the original Ge dimers but gives no information on chemical identity of the reconstructed surface. LEED intensities further suggest the presence of anti-phase boundaries between

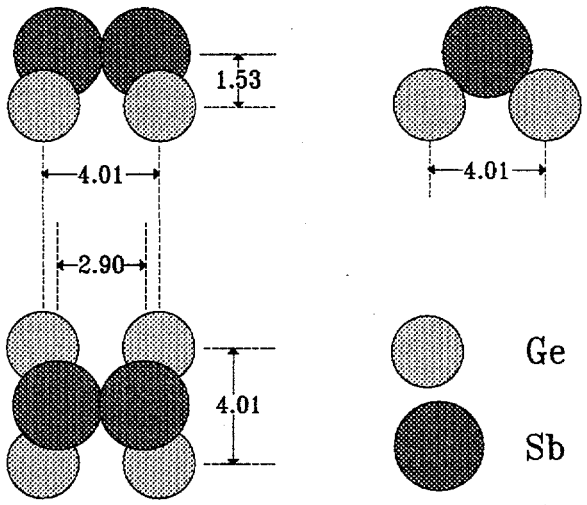

Figure 34. The geometric model of the Sb dimer formed on the Ge(100) surface. Both the top and side views of a single dimer are shown. The atoms are drawn to scale, with the radii being given by the covalent radius of the respective atoms in the bulk.

coherent 2x1 domains of Sb dimers. PES core-level lineshapes indicate that the Ge dimer is removed and that the Sb resides on the surface. SEXAFS shows that the bonding is indeed covalent, as predicted by the Sb dimer model. Due to a lack of information regarding coordination numbers, bond directions cannot be determined from SEXAFS spectra amplitude analysis. It is only when all these results are combined that the interfacial structure becomes clear.

Analysis of SEXAFS spectra determined the Sb-Sb dimer bond length to be 2.91±0.06 Å and the Sb-Ge bond length to be 2.58±0.06 Å. The Sb dimer geometry is shown in Fig. 34. Each Sb atom is bonded to one other Sb and two other Ge atoms. Core-level PES shows the same correlation between electronic and geometric structure as the Sb-Si(100) system. Formation of Sb dimers along with the corresponding removal of Ge dimers manifests itself in the electronic structure as the removal of the surface component of the Ge 3d core-level lineshape associated with the Ge dimer atoms. As with the Sb-Si(100) system, the Sb dimer model results in a passivated surface in that there are no partially-filled dangling bonds.

The only noticeable difference between the Sb-Ge(100) system and the Sb-Si(100) system is its behavior upon annealing. Unlike the Sb-Si(100) system, the Sb-Ge(100) system does not have as wide a range of temperatures at which a single monolayer will form if more than one monolayer of Sb had initially been deposited. It does appear that there is a stable phase at temperatures very near the desorption temperature. Due to the low amplitude of the SEXAFS and its limited range, k-vector analysis of this data is not reliable. In the next chapter, these results will be discussed and compared to other relevant data from the literature.

5. Results and Conclusions

5.1 Experimental Results

We have performed multi-technique studies of the Si(100)-Sb and Ge(100)-Sb surfaces. A combination of scanning tunneling microscopy (STM), low-energy electron diffraction (LEED), angle-integrated core-level photoemission spectroscopy (PES) and surface-extended X-ray absorption fine-structure (SEXAFS) spectroscopy have been employed in order to determine unambiguously the geometric structure of the Sb overlayer along with the accompanying changes to the substrate electronic structure.

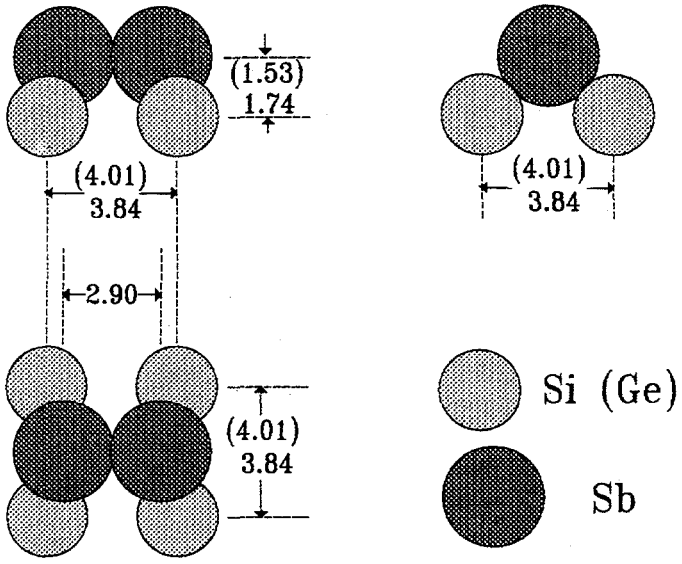

Figure 35. The Sb dimer model. Both top and side views of a single Sb dimer are shown. The distances were determined by SEXAFS spectroscopy. Those in parentheses are for the Sb-Ge(100) surface, while the others correspond to the distances on the Sb-Si(100) surface. Both systems are characterized by covalent bonding, and no partially-filled dangling bonds are present.

It has been determined that the Sb-dimer model describes the overlayer geometry in both systems. This model is characterized by the formation of epitaxial Sb dimers on an unreconstructed substrate. Each Sb atom bonds to one other Sb atom and two substrate atoms, eliminating all of the partially-filled dangling bonds. This geometry, shown in Fig. 35, results in a significant passivation of the surface.

Scanning tunneling microscopy provides a powerful tool for investigating the nature of the overlayer defects present on the Sb-Si(100) surface. Three types of defects are observed. There is some slight second-layer Sb occupation, and also a few regions of presumably bare Si. Two recent studies[82,83] have linked the density of these uncovered regions to the type of impinging Sb. Thermal evaporation results in the deposition of Sb tetramers. These tetramers undergo a complex dissociation path, involving several precursor states. It has been found that the saturation coverage under these conditions is 0.7 monolayer (ML). Slijkerman *et al.*[83] employed a novel "atomic mirror" to provide a source of Sb monomers. This mirror is formed by evaporating Sb tetramers onto a Si wafer held at 650°C. The impinging tetramers undergo thermal dissociation, and the excess Sb desorbs in the form of Sb monomers. Under these conditions, it was found that saturation coverages as high as 0.9 ML could routinely be achieved. Due to the relatively large covalent radius of the Sb atom itself, it seems unlikely that higher coverages can be achieved without sacrificing epitaxial quality, if at all. Because their study did not employ STM, they could not determine how the deposition affects the size of the third type of surface defect, the anti-phase boundary.

The LEED pattern from both the Si(100)-Sb and Ge(100)-Sb surfaces are found to exhibit two-domain 2x1 symmetry. In both cases, however, the higher-order spots are much more diffuse than one would expect from a well-ordered epitaxial layer. We attribute this to the formation of anti-phase boundaries between coherent domains whose dimensions are less than the coherence length of LEED. STM images of the Si(100) surface[71] explicity find the domain size to be on the order of 40 Å, while we infer similar behavior on the Ge(100)-Sb surface by analogy. Because the Ge lattice is 7.04% larger than the Si lattice, it is expected that slightly higher saturation coverages are obtainable, but this has yet to be determined experimentally.

It is well known that geometric and electronic structure are intimately related.

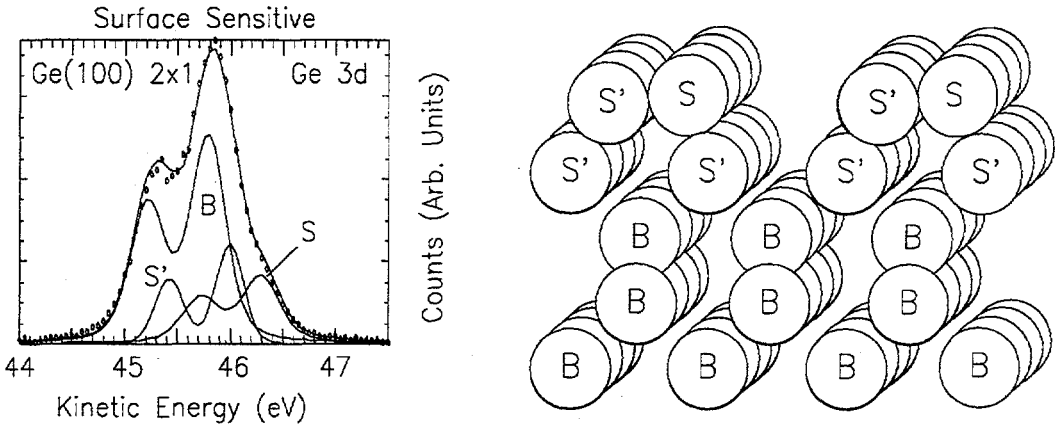

Figure 36. The Si 2p core-level lineshape deconvolution and corresponding atomic structure. The use of multiple techniques allows for the assignment of the various resolved substrate core-level lineshape components to specific surface and near-surface atoms. The Ge(100) system is similar.

Angle-integrated core-level PES was employed to investigate this interdependence. Not only was the effort successful in resolving the changes to the substrate core-level lineshape, but the use of multiple techniques allowed for these changes to be associated with specific changes in the bonding arrangements of the surface and near-surface atoms. The clean reconstructed Si(100) and Ge(100) 2x1 surfaces are characterized by core-level lineshapes that are, within our experimental resolution, comprised of three distinct components. While our initial interpretation assigned the high-kinetic-energy peak **S** to both of the atoms in the surface dimer, the second surface peak **S′** with the second atomic layer, and the bulk peak **B** with the third and deeper atomic layers, some recent PES results obtained with state-of-the-art apparatus requires a slight modification of our interpretation.

Recent work performed at MAX Lab in Lund, Sweden, employed a SX-700 plane-grating monochromator and a high-resolution, angle-resolved hemispherical analyser[84] to improve the system resolution to less than 70 meV. This four-fold increase in resolution allowed for the deconvolution of the Si 2p core-level lineshape into five separate components. Based on this deconvolution and comparison to several theoretical works,[85–87] Landemark *et al.*[84] assign the high-kinetic-energy peak **S** to the

higher atom in a slightly buckled asymmetric dimer. They further deconvolve the peak **S'** into two components. These they associate with both the down dimer atom and the second atomic layer. This arrangement is shown in Fig. 36. While our experiment was unable to resolve these many components, this revision does not affect the final conclusions of this work. It is still justified to use the peak **S** as a signature of the substrate surface dimer. The elimination of this signature peak was used in Chapter 4 to support the interpretation of the LEED patterns obtained from the clean reconstructed and Sb-covered vicinal Ge(100) samples: namely, that the absorption of Sb on the Ge(100) 2x1 surface results in the elimination of the Ge surface dimers, and rotates the surface symmetry direction by 90°.

5.2 Other Relevant Systems

Similar behavior has been observed for at least one other Column V adsorbate. The Si(100)-As system has been studied by X-ray standing-wave spectroscopy[59] and STM.[60] It was shown that the As forms dimers on the Si(100) surface in much the same manner at Sb does. The STM images show that As can form much larger coherent domains, without the presence of voids or anti-phase defects. This can be explained by the smaller covalent radius of As when compared to Sb. It seems As is small enough to form epitaxial layers that do not require occasional voids to relieve strain in the overlayer. This is a concrete example that while electron counting and energy considerations would dictate a certain overlayer geometry, size effects can effect the overlayer morphology.

A much more drastic example of this can be seen in the Sb-diamond systems.[17] Diamond is a wide-bandgap, tetrahedrally-coordinated semiconductor, but with a much smaller lattice. The C-C bond is 1.54 Å as opposed to the Si-Si bondlength of 2.35 Å. Core-level PES studies of Sb on C(100) and C(111) indicate that the Sb

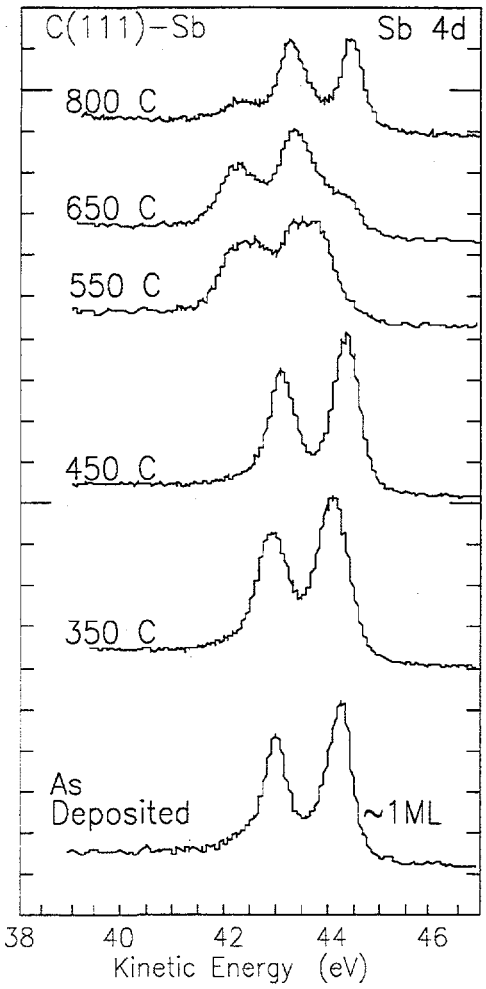

Figure 37. The Sb 4d core-level lineshape from the diamond(111)-Sb system. The Sb 4d core-level lineshape clearly exhibits behavior as a function of anneal temperature drastically different from either the Si(100)-Sb or Ge(100)-Sb systems. While the geometric structure of the interface remains unclear, the data indicate that Sb occupies at least two different absorption sites. Because the Sb atom is much larger than carbon, trimers cannot form.

occupies more than one site on the diamond lattice[17]. This is completely different from any of the Sb-Ge or Sb-Si systems yet studied. One must note that Sb is much too large to form dimers on the C(100) surface or to form trimers on the C(111) surface. While the PES study of Wu *et al.*[17] could not identify the exact geometric structure of the Sb-diamond interface, the data show that the behavior of Sb on diamond is much different from that on either Si or Ge.

5.3 Further Research

This work has presented convincing evidence concerning the geometric and electronic structure of the Si(100)-Sb and Ge(100)-Sb interfaces. The use of multiple techniques has succeeded in providing a level of understanding unattainable by any single technique employed. While the conclusions reached are unambiguous, there are still some unanswered questions. One example is the assumption that the underlying substrate surface can be described by bulk-like atomic positions. It is true that the reconstruction has been eliminated, but the question of substrate relaxation remains to be addressed. The recent refinements of several techniques, specifically X-ray standing-wave spectroscopy[88] and high-resolution X-ray diffraction spectroscopy,[80] now allow for the measurement of the surface relaxations of clean and adsorbate-covered surfaces. These techniques should, and undoubtedly will, be applied to the systems studied in this thesis to determine to what extent the substrate atoms undergo relaxation. Scanning tunneling spectroscopy can be combined with angle-resolved valence-band spectroscopy to provide real-space information on surface states, along with their two-dimensional band structure. By looking at systems of adsorbates and substrates, trends in the periodic table can be investigated. Just one such effect hinted at in this work is that of size. If the adsorbate atoms are too big or too small, how does the system reach equilibrium? What forces dominate on constrained, or frustrated, interfaces? As the techniques used in this work and others are refined, we will achieve previously unimagined degrees of understanding into the forces governing interfacial formation from both the geometric and electronic perspectives.

REFERENCES

1. See E. H. Rhoderick and R. H. Williams, *Metal-Semiconductor Contacts*, 2nd edition (Oxford University Press, 1988), among many good reviews.

2. J.C. Woicik, Ph.D. Thesis, Department of Applied Physics, Stanford University, 1989, unpublished; J.C. Woicik and P. Pianetta, "Studies of Si-Ge Interfaces with Surface EXAFS and Photemmision", in R.Z. Bachrach, ed., Synchrotron Radiation Research: Advances in Surface and Interface Science, vol. 2 (Plenum, 1992) pp 211-266.)

3. T. Abukawa, C.Y. Park, and S. Kono, Surf. Sci. **201**, L513 (1988).

4. The term *covalent* is somewhat vague. The covalent radius is system and coordination dependent. In this thesis, the covalent radius of an atom is defined to be the one half the bond length found in the bulk material. In general, this need not be a unique number, as is the case for carbon. It the cases of Si, Ge, and Sb, this definition does yield a unique value.

5. M. Copel and R.M. Tromp, Appl. Phys. Lett. **58**, 2648 (1991).

6. M. Horn-von Hoegen, F.K. LeGoues, M. Copel, M.C. Reuter, and R.M. Tromp, Phys. Rev. Lett. **67**, 1130 (1991).

7. H.J. Osten, G. Lippert, and J. Klatt, J. Vac. Sci. Technol. B **10**, 1151 (1992).

8. D.J. Eaglesham, F.C. Unterwald, and D.C. Jacobson, Phys. Rev. Lett. **70**, 966 (1993).

9. J.R. Patel, P.E. Freeland, J.A. Golovchenko, A.R. Kortan, D.J. Chadi and G.X. Quain, Phys. Rev. Lett. **57**, 3077 (1986).

10. B.N. Dev, G. Materlik, F. Grey, R.L. Johnson and M. Clausnitzer, Phys. Rev. Lett. **57**, 3058 (1986).

11. T. Nakayama, Y. Tanishiro and K Takayanagi, Surf. Sci. **273**, 9 (1992).

12. V.S. Vavilov, E.A. Konorova, E.B. Stepanova, and E.M. Trukham, Sov. Phys. Semicond. **13**, 636 (1976).

13. J.W. Glessener, A.A. Morrish and K.A. Snail, J. Appl. Phys. **70**, 5144 (1991).

14. H.-J. Scheibe, A.A. Gorbunov, G.K. Baranova, N.V. Klassen, V.I. Konov, M.P. Kulakov, W. Pomps and A.M. Prokhorov, Thin Solid Films **189**, 283 (1990).

15. C.B. Collins, F. Davanloo, E.M. Juengerman, W.R. Osborn, D.R. Jander and T.J. Lee, Texas Journal of Science **41**, 343 (1989).

16. J. Krishnaswamy, A. Rengan, J. Narayan, K. Vedam and C.J. McHargue, Appl. Phys. Lett. **54**, 2455 (1989).

17. J. Wu, M. Richter, J. Terry, X. Yang, R. Cao, P. Pianetta and I. Lindau, Mat. Res. Soc. Symp. Proc., 207, "Novel Forms of Carbon" 407 (1992).

18. G. Binnig, H. Rohrer, Ch. Gerber, and E. Weibel, Appl. Phys. Lett. **40**, 178 (1982).

19. Complete air STMs are now available from several manufacturers for a bit under $100K. Vacuum STMs cost more, due to the added complexity of manufacturing an item compatible with ultra-high vacuum. These systems typically sell for over $100K.

20. J. Tersoff and D. Hamann, Phys. Rev. B **31**, 2 (1985).

21. The Stanford Synchrotron Radiation Laboratory (SSRL) is operated by Stanford University for the U.S. Government Department of Energy, Office of Basic Energy Science, Division of Shemical Sciences.

22. Michal P. Green, Ph.D. Thesis, Department of Applied Physics, Stanford University, 1990, unpublished.

23. P.H. Citrin, P. Eisenberger and R.C. Hewitt, Phys. Rev. Lett. **41**, 309 (1978).

24. J. Stöhr, D. Denley and P. Perfetti, Phys. Rev. B **18**, 4132 (1978).

25. J. Stöhr, Japan. J. Appl. Phys. **17**, 217 (1978).

26. This is not strictly true. Both ion yield and fluorescent photon yield have been used in SEXAFS experiments. Usually electrons are collected because of the high relative counting rates. No matter what particle is detected, the basic EXAFS mechanism requires scanning the photon energy over an absorption edge, and is still chemically specific. For an excellent discussion of the various detection schemes please see J. Stöhr, R. Jaeger, and S. Brennan, Surface Science **117**, 503 (1982).

27. H. Winick and S. Doniach, eds. *Synchrotron Radiation Research*, (Plenum Publishing Corp. 1980).

28. J.W. Rabalais, *Principles of Ultraviolet Photoelectron Spectroscopy* (John Wiley and Sons, 1977).

29. B. Feuerbacher, B. Fitton and R.F. Willis, eds., *Photoemission and the Electronic Properties of Surfaces*, (John Wiley and Sons, 1978).

30. P.A. Lee and J.B. Pendry, Phys. Rev. B **11**, 2795 (1975).

31. E.A. Stern, Phys. Rev. B **10**, 3027 (1974).

32. F.W. Lytle, D.E. Sayers and E.A. Stern, Phys. Rev. B **11**, 4825 (1975).

33. N.C.N. Berglund and W.E. Spicer, Phys. Rev. **136**, A1030 (1964).

34. J. Lambe and R.L. Jaklevic, Phys. Rev. **165**, 821 (1968).

35. D.P. Smith and G. Binnig, Rev. Sci. Instrum. **57**, 1688 (1986).

36. Sang-Il Park, PhD Thesis, Department of Applied Physics, Stanford University, 1986, unpublished.

37. S. Park and C.F. Quate, Rev. Sci. Instrum. **58**, 2010 (1987).

38. J. Stöhr, V. Rehn, I. Lindau and R.Z. Bachrach, Nucl. Instr. and Methods **152**, 43 (1978).

39. R.M. Feenstra, J.A. Stroscio, J. Tersoff, and A.P. Fein, Phys. Rev. Lett. **58**, 1192 (1987).

40. J. Bardeen, Phys. Rev. Lett. **6**, 2 (1961).

41. C. Herring, Seminar on Tunneling, given at Stanford University, September 1986 to March 1987.

42. The potential outside of a solid must obey Laplace's Equation, $\nabla^2\phi = 0$. This implies, using the notation employed in the text, that $\phi_{k_\parallel} \propto e^{-k_\parallel z}$. Using this as the potential in Eq. (2.19) and applying the WKB approximation a slightly modified Eq. (2.20) results, $f_{k_\parallel} \propto e^{-\int^z \sqrt{k_\parallel^2+(V(z)-E)^2}dz}$. In the limit that $V(z)$ is a constant, we recover the expression presented in the text.

43. P. H. Citrin, Phys. Rev. B **31**, 700 (1985).

44. J. Stöhr and R. Jaeger, J. Vac. Sci. Technol., **21**, 619 (1982).

45. B.K. Teo and P.A. Lee, J. Amer. Chem. Soc., **101**, 2815 (1979).

46. While this is not strictly true for cases where the symmetry is less than threefold, in practice the assumption can be made due to averaging over multiple domains.

47. J.C. Woicik, T. Kendelewicz, K.E. Miyano, C.E. Bouldin, P.L. Meissner, P. Pianetta, and W.E. Spicer, Phys Rev. B **43**, 4331 (1991).

48. J.C. Woicik, T. Kendelewicz, K.E. Miyano, P.L. Cowan, C.E. Bouldin, P. Pianetta, and W.E. Spicer, Phys. Rev. B **44**, 3975 (1991).

49. J.J. Yeh and I. Lindau, At. Data Nucl. Data tables **32**, 1 (1985).

50. A very good treatment of scattering of electrons in solids along with the interaction of light with matter can be found in C. Kittel, *Introduction to Solid State Physics,* 6^{th} edition, pp 310-313, (John Wiley and Sons, NY 1986).

51. J. C. Woicik, P. Pianetta, and T. Kendelewicz, Phys. Rev. B **40**, 12463 (1989).

52. T. Kendelewicz, K.E. Miyano, R. Cao, J.C. Woicik, and W.E. Spicer, Surf. Sci. Lett. **220**, 726 (1989).

53. S.H. Lee, P.K. Bhattacharya, S.W. Chung, J.X. Zhou and E. Gulari, J. Elect. Mat. **22**, 409 (1993).

54. D.H. Rich, T. Miller, G.E. Franklin, and T.-C. Chaing, Phys. Rev. B **39**, 1483 (1989).

55. D.H. Rich, F.M. Leibsle, A. Samsavar, E.S. Hirschorn, T. Miller, and T.-C. Chaing, Phys. Rev. B **39**, 12758 (1989).

56. S.A. Barnett, H.F. Winters, and J.E. Greene, Surf. Sci. **165**, 303 (1986).

57. P. Mårtensson, G. Meyer, N.M. Amer, E. Kaxiris and K.C. Pandy, Phys. Rev. B **42**, 7230 (1990).

58. H.B. Eldwijk, D. Dijkkanp, E.J. van Loenen, Phys. Rev. B **44**, 4738 (1991).

59. J. Zegenhagen, J.R. Patel, B.M. Kincaid, J.A. Golovchenko, J.B. Mock, P.E. Freeland, R.J. Malik, and K.G. Huang, Appl. Phys. Lett. **53**, 252 (1988).

60. R.S. Becker, T. Klitsner, and J.S. Vickers, J. Microsc. **152**, Pt. 1, 157 (1988).

61. J. Cerino, J. Stöhr, and N. Hower, Nucl. Instrum. Methods **172**, 227 (1980).

62. G.J. Lapeyre and J. Anderson, Phys. Rev. Lett. **35**, 117 (1975).

63. J. Stöhr, R. Jaeger, G. Rossie, T. Kendelewicz, and I. Lindau, Surf. Sci. **134**, 813 (1983).

64. The STM employed in this study uses only proportional feedback. This signal is then low pass filtered, and sent on to the piezo scanner. This low pass filtering of the feedback signal makes the feedback behave like an integrating feedback loop for times small compared to the cut-off frequency of the low pass filter. This results in a STM that is very stable on atomically smooth surfaces due to the filtering action of the low pass filter. Yet it is prone to tip crashes on rough or clustered surfaces. State-of-the-art STMs now use a combination of proportional, integrated and derivative feedback to maximize the dynamic range on the instrument while allowing routine imaging of quite diverse samples.

65. G.V. Hansson, R.Z. Bachrach, R.S. Bauer and P. Chiaradia, Phys. Rev. Lett. **46**, 1033 (1981).

66. Y. Terada, T. Yoshizuka, K. Oura and T. Hanawa, Surf. Sci. **114**, 65 (1982).

67. J. Stöhr and R. Jaeger, J. Vac. Sci. Technol. **21**, 619 (1982).

68. Please see Chapter 2 for a more complete description of the tunneling process.

69. This work is described in detail in the next chapter.

70. N. Esser, D.R.T. Zahn, C. Müller, W. Richter, C. Stephens, R. Whittle, I.T. McGovern, S. Kulkarni and W. Braun, Appl. Surf. Sci. **56-58**, 169 (1992).

71. J. Nogami, A.A. Baski and C.F. Quate, Appl. Phys. Lett. **58**, 475 (1990).

72. Linus Pauling, *The Nature of the Chemical Bond* (Cornell University, Ithaca, NY, 1939).

73. R.T. Sanderson, *Chemical Bonds and Bond Energy* (Academic, New York, 1971).

74. J.C. Woicik *private communication.*

75. D.-S. Lin, T. Miller, and T.-C. Chiang, Phys. Rev. Lett. **67**, 2187 (1991).

76. R. Cao, X. Yang, J. Terry, and P. Pianetta, Phys. Rev. B 45, 13749 (1992).

77. R. Rossmann, H.L. Meyerheim, V. Jahns, J. Weaver, W. Moritz, D. Wolf, D. Dornisch and H. Schulz, Surf. Sci. **279**, 199 (1992) and references therein.

78. J.A. Kubby, J.E. Griffith, R.S. Becker, and J.S. Vickers, Phys. Rev. B **36**, 6079 (1987) and references therein.

79. J.E. Griffith, P.E. Wierenga, R.S. Becker and J.S. Vickers, J. Vac. Sci. and Technol. A **6**, 493 (1988).

80. M. Lohmeier, H.A. van der Vegt, R.G. van Silfhout, E. Vlieg, J.M.C. Thornton, J.E. Macdonald and P.M.L.O. Scholte, Surf. Sci. **275**, 190 (1992).

81. R. Cao, X. Yang, J. Terry and P. Pianetta, Appl, Phys. Lett. **61**, 2347 (1992).

82. Y.W. Mo, Phys. Rev. Lett. **69**, 3643 (1992).

83. W.F.J. Slijkerman, P.M. Zagwijn, J.F. van der Veen, D.J. Gravesteijn and G.F.A. van de Walle, Surf. Sci. **262**, 25 (1992).

84. E. Landemark, C.J. Karlsson, Y.-C. Chao and R.I.G. Uhrberg, Phys. Rev. Lett. **69**, 1588 (1993).

85. D.J. Chadi, Phys. Rev. Lett. **43**, 43 (1979).

86. J. Ihm, D.H. Lee, J.D. Joannopoulos and J.J. Xiong, Phys. Rev. Lett. **51**, 1872 (1983).

87. T. Tabata, T. Aruga and Y. Murata, Surf. Sci. **179**, L63 (1987).

88. J.C. Woicik, T. Kendelewicz, K. Miyano, P. Cowan, M. Richter, B. Carlin, C. Bouldin, P. Pianetta and W.E. Spicer, J. Vac. Sci. Technol. A, **10**, 2041 (1992).